A COMPREHENSIVE STUDY OF MATRIX FRACTURE MECHANISMS IN FIBER-REINFORCED CERAMIC MATRIX COMPOSITES

A. S. D. Wang and M. W. Barsoum
Drexel University
Philadelphia, PA 19104

FINAL TECHNICAL REPORT
AFOSR Grant No. ~~90-0712~~ 90-0173

for

Air Force Office of Scientific Research
Bolling AFB, DC 20332

June 1993

DISCLAIMER NOTICE

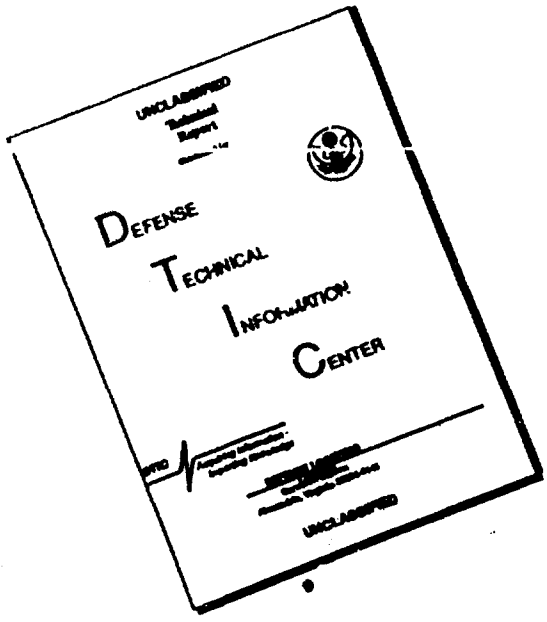

THIS DOCUMENT IS BEST QUALITY AVAILABLE. THE COPY FURNISHED TO DTIC CONTAINED A SIGNIFICANT NUMBER OF PAGES WHICH DO NOT REPRODUCE LEGIBLY.

REPORT DOCUMENTATION PAGE

Form Approved
OMB No. 0704-0188

1. AGENCY USE ONLY (Leave blank)	2. REPORT DATE	3. REPORT TYPE AND DATES COVERED
	30 June 1993	Final Tech. Rep. 15 Feb. 90, 30 Apr. 93

4. TITLE AND SUBTITLE
A comprehensive study of Matrix Fracture Mechanics in Fiber-Reinforced Ceramic-Matrix Composites

5. FUNDING NUMBERS
AFOSR -90-~~0712~~
90-0172

6. AUTHOR(S)
A.S.D. Wang and M.W. Barsoum

7. PERFORMING ORGANIZATION NAME(S) AND ADDRESS(ES)
Drexel University
Philadelphia, PA 19104

8. PERFORMING ORGANIZATION REPORT NUMBER
N/A

9. SPONSORING/MONITORING AGENCY NAME(S) AND ADDRESS(ES)
AFOSR/NA
Bolling Air Force Base
Washington, DC 20332

10. SPONSORING/MONITORING AGENCY REPORT NUMBER

11. SUPPLEMENTARY NOTES

12a. DISTRIBUTION/AVAILABILITY STATEMENT
Distribution Unlimitted

12b. DISTRIBUTION CODE

13. ABSTRACT (Maximum 200 words)

This final technical report summarizes the activities, accomplishment and research results obtained under the research grant AFOSR-90-0712, which covered the period from 15 February 1990 to 30 April 1993.

The main objective of the research is to study the physical mechanisms of matrix microcracking which constitutes the fundamental cause for the toughness and strength properties in fiber-reinforced ceramic-matrix composites. Major results summarized in this report include (1) fabrication of the test specimens with controlled microstructural variables; (2) laboratory tests of matrix microcracking with in-situ and real-time monitoring; and (3) formulation of a simulation model and modeling results.

A list of publications that have resulted from this research is included in this report.

14. SUBJECT TERMS	15. NUMBER OF PAGES
	80
	16. PRICE CODE

17. SECURITY CLASSIFICATION OF REPORT	18. SECURITY CLASSIFICATION OF THIS PAGE	19. SECURITY CLASSIFICATION OF ABSTRACT	20. LIMITATION OF ABSTRACT
unclassified			

TABLE OF CONTENTS

1. INTRODUCTION

This Final Technical Report contains the summary of the research results obtained under the University Research Initiative (URI) Grant AFOSR-90-0712, entitled "A Comprehensive Study of Matrix Fracture Mechanisms in Fiber-Reinforced Ceramic Matrix Composites". The URI Grant covered the period from 15 February 1990 to 30 April 1993.

1.1 Research Objective.

The impetus of the research stems from the Air Force's needs for a class of structural materials that can function in severe temperature environments; and fiber reinforced ceramic matrix composites have thus become a prime subject for research and development. Although some ceramics are thermally stable up to a temperature beyond 2000 ^{o}C, they are invariably brittle and lack the required strain capability as a structural material. However, when it is reinforced with a network of equally thermal stable, high strength and (relatively) high strain fibers, the brittle nature of the ceramic matrix may be circumvented and the toughness of the composite increased. But the toughening mechanisms due to fiber reinforcement can be influenced by a host of intrinsic and extrinsic factors, such as composite processing, placement of the fibers, interfacing with the matrix, and the mechanical interactions that occur in the composite microstructure under the applied loading. Hence, there is a need to identify and characterize these influencing factors; to establish their ranges of influence; and to include them in a generic model that can describe the toughening mechanisms and provide a predictive capability.

Thus, the objective of the present research is to conduct a comprehensive study towards understanding the complex toughening mechanisms in fiber reinforced ceramic matrix composites. As the necessary first step, the present study focuses on the physical nature of matrix microcracks and the factors influencing their initiation. The scope of the research thus entails composite processing, testing of matrix microcracking, identification/characterization of the influencing factors, and the construction of a predictive model suitable for numerical simulation of the matrix microcracking processes as observed in the tests. All composites so studied are limited to unidirectionally continuous filament-reinforced ceramic systems.

1.2 Research Approach.

The approach taken in the study is one involving interactive efforts in experiment, theorization and simulation. The common thread linking these efforts is the control and variation of those parameters in processing, material selection and loading which are deemed important in the matrix microcracking processes.

The control and variation of the influencing parameters begins with composite fabrication, where several material and geometric factors known to influence matrix microcracking are varied. Specifically, through the selection of different fiber-matrix combinations, mismatch of the thermal and mechanical properties between fiber and matrix is controlled; through the selection of fibers of

different sizes (but with the same matrix), local fiber geometry is altered; through the selection of matrices of different toughness properties (but with the same fiber), matrix influence on localized fracture is controlled; through treatment of the fiber surface prior to fabrication, the fiber-matrix interface bonding strength is controlled; and through a unique processing method, the fiber volume content in each of the composite systems is varied uniformly from null to about 50%. Furthermore, in order to establish the influence range of each of the controlled parameters, a statistical data base in each case is generated.

As a result, the test program becomes extensive and comprehensive. In particular, testing and instrumentation are designed to emphasize in-situ observations in real-time; so the actual matrix microcracking mechanisms can be delineated visually and a complete record for the cracking process obtained as a function of the applied loading. Generic model is constructed based on the observe microcracking mechanisms and their relationship with respect to the influencing factors; the successful model is then applied to simulate each of the test cases by means of a numerical procedure (i.e, the finite element method). The following provides a brief outline of the various tasks performed in the study.

1.3 Research Tasks.

During the three-year period of the present research, numerous tasks have been performed. Key areas of research conducted in the period are briefly discussed below:

In-House Composite Fabrication. This task is the keystone of the present research, in that composite samples of both quality and quantity must be routinely made for testing. As is mentioned, selection of the matrix, fiber and interface treatment is so large and variation of fiber volume content in the composites changes from null to 50%, the number of test samples needed is considerable. During the first two years of the present study, much of our effort is devoted in developing the fabrication procedures to insure sample quality, in addition to preparing the required sample population.

Testing and Instrumentation. With the focus placed on the "initiation mechanisms" of matrix microcracking in unidirectional filament reinforced systems, the test condition chosen for all samples is tension loading along the fiber direction. This is achieved by 3-point bending test of a slender beam. The difficulty associated with the test is that (a) to capture the moment of microcrack initiation; and (b) to follow crack progression in the composite microstructure during loading. This difficulty is further compounded by the fact that some of the tests must be conducted in high temperature conditions. As will be discussed later in this report, special test fixture and real-time observation instrumentations are developed during the research period.

Modeling and Simulation. To develop a theoretical model that can correctly link the microstructure, the influential factors and the applied loading to the physical events of matrix microcracking is the central piece of the present research. Since the desired model must be based on mechanics principles and the actual cracking mechanisms, correlation between the model and

experiment is important. The correlation is provided by numerical simulation of the actual tests, so that results from the simulation can be compared directly with experiment; any deficiency of the theoretical model is amended through correlative iterations. The value of such a model lies not only in its predictive capability of matrix microcracking, but also in its explicit inclusion of the various influencing factors which play a role in the toughening mechanisms of the composites.

Baseline Property Characterization. In order to provide the necessary input data in the numerical simulation of the tests, a considerable amount of effort is devoted to obtain the relevant material properties for the matrices and the fibers used. Although most of the thermoelastic constants for the matrices and the fibers at room temperature can be determined by routine methods, exceptions are abound. Among the most difficult ones are (a) the measurement of the thermal expansion coefficients of the fibers; and (b) the measurement of the fracture toughness of the bulk matrices in high temperature. The former is needed to assess the thermal residual stress state of the composites, while the later provides the necessary material condition for matrix microcracking.

Interface Mechanics Study. Fiber-matrix interfacing is a key parameter governing the load-transfer mechanisms in composite materials. Proper mechanics characterization of the interface is essential for the understanding of the failure processes and the toughening mechanisms in composites. An effort is made to rigorously study interface mechanics; extensive experiment and theoretical modeling are perform. Details on this effort are presented later in this report.

1.4 The Research Team.

The following faculty, graduate students and research associates have participated in the research as a team:

* A. S. D. Wang (PI), Soffa Professor of Mechanical Engineering
* M.W. Barsoum (Co-PI), Associate Professor of Materials Engineering
* T. M. Tan (Co-PI, departed Feb. 92), Associate Professor of Mechanical Engineering
* P. Kangutkar, graduate student (graduated/Ph.D. Sept. 91), Materials Engineering
* X. G. Huang, graduate student (graduated/Ph.D. Feb. 92), Mechanical Engineering
* P. V. Kishore, graduate student (graduated/Ph.D. Mar. 93), Mechanical engineering
* T. Dong, graduate student (Sept. 91-Mar. 93 with M.S.), Materials Engineering
* H. M. Chou (departed, June. 91), Post-doctorate Fellow, Materials engineering
* J. C. Gong (departed, Sept. 91), Post-doctorate Fellow, Mechanical Engineering
* A. Elkind (Sept. 91-Mar. 93), Post-doctorate Fellow, Materials Engineering

The team is organized into five task-groups, each is assigned to specified responsibility as follows: (1) fabrication and testing (Barsoum, Kangutkar, Dong); (2) thermoelastic properties of fibers, matrices and composites (Barsoum, Kangutkar, Elkind); (3) fabrication and testing of interface properties (Chou, Tan, Gong); (4) model and simulation of interface mechanics (Wang, Kishore); and (5) modeling, simulation and correlation of matrix microcracking (Wang, Huang).

A. S. D. Wang is the overall manager of the research team.

1.5 Research Reporting.

Throughout the course of the present research, major findings are reported via several technical media: (a) AFOSR Annual Technical Reports; (b) Ph.D. Dissertations; (c) Archival Journal Papers; (d) Proceeding of Technical Symposia; (e) Presentation at Technical Conferences; and (f) Invited Seminar at Universities and Research Institutes. A complete bibliography resulting from the present research is contained in **Section 4**.

In what follows, a brief summary of the major results obtained in the research is given. Whenever possible, specific details are referred to the appropriate publications that are listed in **Section 4**.

2. MAJOR RESULTS AND DISCUSSIONS

2.1. Composite Fabrication.

During the first year of this research, an in-house processing facility is setup to fabricate unidirectional continuous fiber reinforced ceramic matrix composites with the desired quality. The processing procedure is then followed to fabricated numerous test samples for subsequent matrix microcracking study. A brief outline of the fabrication aspects of the research is given below:

Fabrication Procedure. *The composite* fabrication technique adopted in this research has been well established in the open literature (see Ref.[B-1] for specific details). For purpose of discussion, the general procedure is as illustrated in Fig.1. In brief, matrix material (glass) in powder form is mixed with a polymer slurry; the reinforcing fiber is then made to pass through the slurry and the slurry coats the fiber to form a uniform surface layer; the coated fiber is next exposed to a ultraviolet light source which cures the polymer slurry coating; the coated fiber is wound uniformly onto a drum to form a collimated prepreg tape; from the prepreg, a green unidirectional laminate is made; the green laminate is then heated in air at 500 ^{o}C to burn out the polymer in the coating, leaving the glass powder adhering to the fiber surface; the laminate is finally placed in a graphite die and hot-pressed in vacuum to form a consolidated composite plate.

The fiber-volume content in the composite plate is determined by the amount of glass powder used in the polymer slurry. Fiber contents from 0 to 50% are made for each of the selected fiber-matrix combinations. Composites of zero fiber content are simply the bulk matrix with any fiber, hot-pressed under the same condition as those with fibers.

Selection of Matrices. Three matrix materials are selected for fabrication of composite samples; and these are: (a) 7740 borosilicate; (b) 1723 aluminosilicate; and (c) zircon. All come in powder form and are adaptive to the fabrication procedure as outline before. The rationale for the selection is based on their contrasting material properties, especially the tensile modulus, tensile strength, fracture toughness and the strain point (the phase change temperature from liquid to solid

or vise versa); and it is believed that the effect of these contrasting properties on matrix cracking should be detectable both in experiment and in theory. The following table lists some of the baseline properties of the three selected matrices.

	7740	1723	zircon
Modulus (GPa)	63	83	195
TEC (10^{-6}/C)	3.2	4.6	4.2
K_{Ic} (MPa$\sqrt{m}$)	0.75	0.8	2.5
Ten. strength (MPa)	80	35	265
Strain point (^{o}C)	520	650	900

Selection of Fibers. Four fiber systems are selected for fabrication of composite samples and they are (a) SCS-6 SiC; (b) SCS-9 SiC; (c) Nicalon SiC; and (d) HMU graphite. The SCS-6 and SCS-9 fibers are monofilaments, while the Nicalon and HMU carbon fibers come in tow. The following table lists some of their contrasting properties:

	SCS-6	SCS-9	Nicalon	HMU-C
Modulus (GPa)	400	390	200	380
TEC (10^{-6}/C)	6.5	6.5	3.1	0.1
Diameter (μm)	75	35	8	4

Similarly, the contrasting properties in these fibers are believed to cast contrasting effects on matrix microcracking, detectable in experiment and in theoretical predictions.

Interface Treatment. To study the effect of interface bonding on matrix microcracking, the SCS-6/7740 borosilicate composite is selected for interface treatment. The treatment procedure involves heating the SCS-6 fiber in air at 600^{o}C for about 1 minute, to achieve a thin oxidized surface layer; upon processing into composite, the oxidized surface layer of the fiber provides a much stronger interface bonding. By means of the fiber pullout test, fiber so treated results in an interface shear strength exceeding 100 MPa, while the untreated fiber provides only about 8 MPa. The details of the surface treatment and the subsequent interface shear tests are reported in Ref. [C-2].

Composite Systems Fabricated. Eight composite systems are fabricated during the research period, using the three selected matrix materials and the four selected fibers. These are listed as follows:

1. SCS-6/7740 (without interface treatment)
2. SCS-6/7740 (with interface treatment)

3. SCS-9/7740
4. Nicalon/7740
5. HMU-C/7740
6. SCS-6/1723
7. Nicalon/1723
8. SCS-6/zircon

In each system, the fiber volume content is varied uniformly from 0% to approximately 50%. This resulted in fabricating some 16 plates of 4"x4" in size for each composite system (from each plate, 5 to 6 test specimens could be made). More than 600 test samples in all are fabricated and tested during the research period.

Detailed documentation for the processing, fabrication and sample preparation is contained in the Ph. D. thesis by Kangutkar [B-1].

2.2. Matrix Microcracking Test Specimens and Procedures.

Matrix microcracking tests conducted in this research use the 3-point-bend loading method where matrix microcracking events are induced on the tensile face of the 3-point specimen under center loading. The test specimens are in the form of a beam with the nominal dimensions of 60 mm long, 5 mm wide and 2 mm deep. Specimen preparation before testing is a critical in terms of the quality of test data. For instance, each specimen must be finely polished in order to eliminate flaws and excess glass on the surface and near the corners. Details for the specimen preparation are fully described in Ref. [B-1].

Most of the 3-point bend tests are conducted under room temperature; a number of selected composite systems are also tested in higher temperatures. In order to monitor the matrix cracking events in real-time and in-situ, two different recording methods are used, depending on the test temperature. A brief outline of these two methods is given as follows:

1. At room temperature, tests are conducted inside the chamber of a scanning electronic microscope (SEM). A specially designed test fixture is housed inside the SEM, with a remove load-control devise; visual details of matrix microcracking could be observed in-situ under the power of the SEM up to 1000x. The test fixture used is schematically illustrated in Fig. 2.

2. At temperatures higher than room temperature, each test specimen is prepared with a thin gold-film sintered on its tensile surface prior to testing, as illustrated in Fig. 3. Tests are then conducted in a thermal chamber affixed in the loading train on a MTS testing machine. During the test, a devise is used to measure the electric resistance of the gold film in the direction along the beam. When matrix microcracking occurs in the specimen and breaks the gold-film, the electrical resistance of the film increases abruptly. The corresponding load is recorded and used to compute the critical tensile stress for matrix microcrack initiation.

The SEM in-situ test provides the visual details of the matrix cracking mechanisms at the fiber-matrix-interface scale. For example, one of the major findings in this research is that matrix

microcracking initiates generally within a local fiber spacing as an isolated event; as the applied load increases, more such local events occur within other fiber spacings. Localized interface debonding then forms near the matrix cracking sites at higher load levels; these local matrix microcracks eventually link up through the interface debonds, resulting in a larger and zigzagged matrix crack across the width of the test sample. A schematic of the cracking initiation and linking sequence is illustrated in Fig. 4. This finding is important in determining the mechanisms of matrix cracking and in guiding the development of the cracking simulation model.

A typical matrix microcrack initiation stress (MCIS) data is shown in Fig. 5 from testing the SCS-6/7740 specimens (without interface treatment) in room and higher temperatures. The MCIS data is plotted versus the fiber volume content V_f of the test specimens, with V_f varying from 0 to 0.5. Though the test data is quite scattered they do provide both a statistical basis and a definitive behavioral tend, useful for the eventual validation of the developed simulation model.

Again, the experimental aspects regarding the tests and test data analysis are detailed in the thesis of Kangutkar [B-1].

2.3. Simulation Model for Matrix Microcracking.

The theoretical framework for modeling matrix microcracking is first conceived in 1988. The original idea is further developed during this research due to the extensive experiment. Most of the details in the model development are described in the Ph. D thesis by Huang, Ref.[B-2].

The developed model differs from models of the past in one major aspect. Namely, the present model describes the composite microstructure at the fiber-matrix interface scale and accounts for the effect of material defects both in the matrix and on the matrix-fiber interface. Fig. 6 shows the schematics of the matrix microcracking model and the input parameters included in the model. Specifically, these parameters include: the thermoelastic moduli of the matrix and the fiber; the composite processing temperature parameter; the fracture toughness of the matrix; the geometrical details of the local microstructure (e.g. fiber diameter and fiber spacing); and the representation of local defects both in the matrix and on the fiber-matrix interface.

Clearly, not all of the parameters are deterministic; some are actually random in nature. This causes uncertainty in the input data into the model and a bounding approach is developed to compliment the model. Nevertheless, the model is still capable of describing the complex interactions amongst the local defects that are situated in an evolving composite microstructure, and actually mimicking the matrix crack process under the applied loading as it would in a real test situation. Thus, the model can provides a description of the actual cracking process in quality and quantity, although the augmentation of the model must be complimented by a bounding technique due to the uncertainty involved in the input parameters. Details of these development are found in [B-2] and [C-4].

The successful model is used to perform two major tasks. The first is a parametric study on matrix microcracking initiation. The study is quite extensive in that it examines the microcracking

behavior as it is influenced by all the parameters included in the simulation model. The study not only establishes the value-ranges for each of the parameters but also allows an examination of the intricate interactions amongst the parameters. The other task concerns the simulation of the actual test cases (about 600 cases) and the prediction of the MCIS. The latter is used in comparison with the experiment.

A typical theoretical-experimental comparison is shown in Fig. 7, where the MCIS data from testing and simulation of the SCS-6/7740, SCS-6/1723 and SCS-6/zircon specimens are shown plotted versus the fiber volume fraction, V_f. It is seen that the agreement between theory and experiment is rather good. In fact, close comparison of MCIS between the predicted and the tested results are consistently obtained from all the 8 different composite systems, see [B-2]. This is rather remarkable in view of the diversity in the microstructure features exhibited in the differing composite systems.

2.4 Major Findings from Matrix Microcracking Results.

From over 600 test data and in conjunction with the results from model simulations, a number of interesting findings are obtained. A brief discussion on some of the major findings is presented in the following:

Test Specimen Surface Polishing. By finely polishing the test specimens before testing, it helps to eliminate surface defects and excess matrix; surface defect and excess glass can cause matrix cracking prematurely and result in large data scatter. This is illustrated by the data shown in Fig. 8 where a comparison of the MCIS data is made between the polished and the unpolished SCS-6/7740 specimens. It can be readily seen that surface polishing reduces the scatter in the MCIS data (details of specimen surface polishing is presented in [B-1]). In the discussions that follow, all data presented are from testing polished specimens.

Matrix Microcracking Begins as Isolated Cracks in Fiber Spacings. As has been discussed earlier, the first matrix microcracks are found to form inside the spacing of two adjacent fibers. In general, fiber spacing in a specimen is not uniform due to processing variability; and the first few matrix cracks occur almost always inside the largest fiber spacings. Furthermore, the threshold stress (MCIS) is found to correlate with the value of the fiber spacing in which the crack occurs. This later is illustrated in Fig. 9 which displays the MCIS data from testing 7 SCS-6/7740 specimens. In the first figure the MCIS is plotted against the average fiber spacing on the tensile surface of the specimens (the averaged fiber spacing is tantamount to the averaged fiber volume content, V_f), while in the second figure, it is plotted against the value of the spacing in which the first matrix crack occurs. From the second plot, the trend that the MCIS decreases with increasing the fiber spacing is evident.

This finding indicates the importance of fiber spacing uniformity during composite processing. As an inherent property of the system, fiber spacing always exhibits a certain scatter in its value (see, e.g. the 7 data points in Fig. 9). Lack of sufficient uniformity of fiber spacing

causes scatter in the MCIS values. It is possible that both the MCIS and its scatter may be increased by improving the fiber spacing uniformity during processing. Further discussion on this subject, together with the SEM examination records, can be found in Ref. [B-2].

Small Fiber Is Better Than Large Fiber. From both the parametric study on fiber size and the experiment with fiber size controlled, it becomes evident that systems with fibers of smaller diameter out performs systems with fibers of larger diameter in terms of the MCIS if all the other parameters are kept the constant. Fig.10 shows the MCIS data (plotted against V_f) from testing a group of SCS-6/7740 specimens and a group of Nicalon/7740 specimens; the system with the Nicalon fiber provides substantially higher MCIS than the system with the SCS-6 fiber. Though both fibers are basically made of SiC, the Nicalon has a diameter ranging from 10 to 20 μm (with an average of 16 μm) while the SCS-6 has a diameter of 150 μm. The theoretical average fiber spacing, s depends on the fiber diameter, d and the fiber volume fraction V_f by the relation: $s=d\{\sqrt{[(\sqrt{3}\pi)/(6V_f)]}-1\}$.Thus, for the same V_f, the average fiber spacing is directly proportional to the fiber diameter.

One might also note that the elastic moduli of the Nicalon and the SCS-6 are not the same; the Nicalon is only half as stiff in the longitudinal direction as that of the SCS-6. If the data in Fig. 10 is converted into composite strain instead of stress (see Fig. 11), the advantage exhibited by the Nicalon is even more pronounced. Fig. 12 shows a similar comparison between the SCS-6/1723 and the Nicalon/1723 systems. Here, again, the Nicalon out performs the SCS-6 in terms of matrix cracking strain.

The comparisons presented above, however, are not strictly based on the difference in fiber diameter alone since the Nicalon and the SCS-6 are different fibers in other aspects, such as elasticity, interface bonding characteristics, processing preparation, etc.

In order to circumvent the difficulty associated with these differences, another experiment is conducted in which systems made of the SCS-6 and SCS-9 are fabricated and tested. The two fibers are basically the same in every aspects except that the SCS-9 has a diameter of 70 μm, while the SCS-6 150 μm. When these fibers are coupled with the same matrix (the 7740) and processed under the same condition, the effect of fiber size alone is isolated.

Fig.13 displays the comparison of the MCIS between the SCS-6/7740 and the SCS-9/7740 systems as plotted against V_f, both curves are predicted using the developed simulation model (this prediction is based on the parametric study performed before the procurement of the SCS-9 fiber). The prediction indicates that the SCS-9 fiber out performs the SCS-6 fiber in MCIS.

Fig 14 displays the comparison of MCIS obtained by experiment. In this case, the MCIS data display a considerable scatter; the difference in MCIS between the two systems can still be

discerned in the V_f range above 30%. In this V_f range, the average fiber spacing in the SCS-9 system becomes small enough to effect an increased fiber constraint against matrix microcracking. This is not the case for the SCS-6 system.

It should also be mentioned that the interface bonding strength in the SCS-6/7740 system is about the same as that in the SCS-9/7740 system (this will be further discussed later in this report). Thus, the comparison presented in Fig.14 can be considered as based on the difference in fiber size alone. Overlay of Fig. 13 and Fig.14 will show that the model predicted MCIS by falls reasonably well inside the experimental data band.

Effect of Interface Bonding. The reinforcing fibers will provide a constraining effect on matrix microcracking only if the fiber-matrix interface is adequately bonded. If the interface bonding is weak, the threshold stress for matrix microcracking (MCIS) is generally lowered. A physical explanation with mechanics quantification of the effect is fully described in the simulation model, see Ref. [B-2]. An experiment is also conducted to validate the effect of interface on the MCIS. In this case, composites made of surfaced treated and untreated SCS-6 fibers with the 7740 matrix are fabricated and tested (details for fiber surface treatment are presented in [B-1]; also, in a separate test involving single fiber pullout, the interface shear strength of the untreated fiber is found: τ = 6 - 8 MPa, while that of the surface treated fiber: τ > 100 MPa). Fig. 15 shows the comparison of the measured MCIS from the group with untreated fibers and the group with surface treated fibers; the group with surface treated fibers has substantially higher MCIS than the group without surface treatment.

Effect of Matrix Flaw Size. The fundamental notion that microflaws are present in the matrix phase of the composite and they are the source of matrix microcracking is the basis on which the crack initiation mechanism is modeled. Within that context, the actual identity of the microflaws (size, shape and distribution) cannot be realistically determined. However, as an effective quantity, the microflaws may be considered as being inherent to the matrix material, the interactions with the fibers during processing, post-processing handling, etc. In that sense, they can come as a random variable. It is then argued that the effective size of the flaws must be bounded either by (a) the size of fiber spacing, s and (b) the size of the largest effective flaw in the bulk of the matrix, a,whichever is smaller. The former can be evaluated by knowing the fiber size and fiber volume content; while the latter can be inferred by applying the classical fracture mechanics for brittle crack, assuming that the matrix tensile strength σ_m is determined by the matrix fracture (mode-I) toughness K_{Ic} and the effective flaw size a.

For instance, between the 7740 and the 1723 glasses in bulk, the corresponding K_{Ic} are 0.75 MPa$\sqrt{m}$ and 0.8 MPa$\sqrt{m}$, respectively; the corresponding σ_m are 80 MPa and 35 MPa,

respectively. Thus, the corresponding dominant effective flaw sizes are 60 μm and 300 μm, respectively. This is why the 1723 glass is weaker than the 7740 glass in terms of tensile crack resistance. Hence, if reinforced with the same amount of fiber, the threshold stresses at matrix microcracking initiation can be elevated more significantly in the 1723 system than in the 7740 system.

Fig. 16 shows the comparison of the MCIS as a function of fiber volume content between the SCS-6/7740 and the SCS-6/1723 specimens. The MCIS is increased much more dramatically in the 1723 system due to increase of fiber reinforcement than in the 7740 system. According to the effective flaw concept, the average fiber spacing in the 7740 system is larger than the maximum effective flaw size in the bulk matrix when the fiber volume content V_f is less than 0.3. In that case, the reinforcing fibers are ineffective in constraining the initiation of matrix microcracking. A full discussion on this subject is presented in Ref.[D-3].

2.5 Fiber Pullout Tests and Interface Study.

One of the main tasks performed in this research is to provide the necessary baseline properties in order for model simulation. These properties include the thermoelastic constants of the matrix and fiber material used, the tensile strength properties of the matrix including the mode-I fracture toughness, and the interface properties between the matrix and fiber. Most of these properties can be gathered either from prior studies or from routine characterization tests. The interface property, however, is unique to the particular composite processing in question and the interface property characterization procedure is by no means routine. In fact, a significant effort is made during this research towards the interface study; both experiment and model simulation are conducted. Some key point in this effort will be briefly discussed below.

The Single Fiber Pullout Test. The interface study test program is carried out using the SCS-6/7740, SCS-9/7740 and the Nicalon/7740 systems. It involves fabrication and testing of a large number of single-fiber pullout specimens. The objective of the test program is to examine the underlying mechanisms in the fiber pullout process as well as to determine the actual values of the interface shear strength, τ in all the composite systems. The former provides the physical basis for the development of a fiber pullout simulation model, while the latter is used as input into the matrix microcracking simulation model.

Fig. 17 shows the schematics of the pullout test and Fig. 18 is a photograph of the actual test setup. Test results of the interface shear strength and related discussions are found in Refs. [A-2], [C-1], [C-2] and [H-1].

Three different mechanisms which govern the fiber pulling out motion are identified: (a) purely elastic response when the interface is intact or undamaged; (b) interface debonding near the matrix surface and propagating down the fiber's embedded length; and (c) frictional sliding when the interface is debonded. The mechanisms (b) and (c) may occur separately or concurrently

depending on a number of factors, such as the residual stresses due to processing, the ambient test temperature, etc.

Simulation of Fiber Pullout. A simulation model is developed based on the three mechanisms identified in the fiber pullout tests. The model is then used to sort out the effects of the various influencing factors governing the property of the interface.

The simulation model is formulated on basis of three-dimensional elasticity; and the resulting governing equations are solved using a 'solution-matching' procedure. This procedure is new to the computational mechanics literature and it offers both accuracy and efficiency in simulating the fiber pullout motion. Briefly, the procedure involves the determination of the stresses of the singular field neat the fiber and the stresses in the far-field where loading and boundary conditions are specified; accuracy of the computed stresses and the corresponding fracture quantities are assured by matching the two solutions perfectly within the domain where they overlap.

The developed model and the computational scheme are coded on a high-speed computer to mimic the pullout test with the mechanisms that are identified in the tests, including fiber pulling with perfect interface bonding, interface debonding initiation and propagation and frictional sliding after fiber debonding.

The above development forms the basis of the Ph. D. thesis by Kishore Pochiraju [B-3]; a copy of which has been submitted to AFOSR as a part of our routine reporting. A series of archival papers resulting from this research have either appeared or been submitted for publication in the open literature. A copy of the paper [D-4] which details the stress-fields matching technique is included in the Appendix.

2.6 Thermal Expansion Coefficient of the SCS-6 Fiber. Thermal residual stresses in composites play a significant role in the formation of microscopic damages in the composite. In order to quantify the contribution of the thermal effect to matrix microcracking, determination of the thermal expansion coefficients of the matrix and the fiber is the essential first step. Generally, thermal coefficients of the commonly used materials can be found either from the open literature, or from the material supplier. However, the reliability of such sources cannot be certain. This has been the case in the present research when the SCS-6 fiber is used.

Specifically, the longitudinal thermal expansion coefficient of the SCS-6 filament has a nominal value in the range of 4 to $5.5 \times 10^{-6}/^{o}C$, according reports in the literature. The wide range of the reported values reflects the uncertainty of the source; and it causes difficulty in their use in order to insure the computed thermal residual stresses in the composite with the required accuracy. Thus, an effort is made in this research to independently measure the thermal expansion coefficient of the SCS-6 fiber in the range of 25 to 900 ^{o}C. The experiment itself and subsequent follow-up investigations have uncovered a number of important physical and chemical characteristics of the SCS-6 fiber in high temperature environments. In particular, the thermal expansion coefficient

measured in this research has a value of $6.5 \pm 0.5 \times 10^{-6}/^{o}C$, much higher than any of the reported values. Through a number of direct and indirect checks, it is concluded that the higher value measured is probably correct; the reason for the high value can be attributed to the formation of β-SiC grain growth during high temperature heating, which subsequently changes the overall physical property of the fiber.

The details of the experiment and related discussions on the results are contained in Refs. [C-5], [D-5] and [D-6]. A copy of Ref.[C-5] is included in the Appendix.

3. CONCLUSIONS

In the three years of the present research, we have focussed on achieving the main objective set out at the beginning of the program, which is to first understand and then describe the complex fracture toughening mechanisms in fiber-reinforced ceramic matrix composites. In this context, matrix microcracking is singled out for study because it is the fundamental form of damage in such composites. It is necessary to plan and to execute an experimental program to identify the key factors affecting matrix microcracking and to develop a simulation model that describes the physics of the cracking phenomenon. In the experiment, control of the influencing factors in the test specimens is essential to assess their effects on matrix microcracking; it leads to an extensive specimen fabrication plan. At the same time, a visual (physical) comprehension of the cracking mechanisms at the fiber-matrix interface level is helpful; and it leads to painstaking experimental procedures in order to observe and follow the cracking process in-situ and in real-time.

As for the development of the simulation model, the representation of the composite microstructure and the inclusion of the observed cracking mechanisms and the factors controlling matrix microcracking result in a complex micromechanics model which requires (a) extensive input data which must be complete and accurate; and (b) a suitable numerical routine that can be executed on the computing machine.

It is important to point out that some of the necessary input data are in-situ properties and are not easily determined (such as the interface property). In addition, the basic assumptions based on which the simulation model is developed cannot be all validated through experiment. Thus, the adequacy of the matrix microcracking model can be judged only based on test data collected in the program. In that sense, it may be said that comparison between the test data and the model simulation is quite good and extensive.

Two important areas remain yet to be explored more fully. One area is the study of the linking mechanisms of the isolated matrix cracks; crack-linking is a major energy dissipation mechanism. The other area is the study of high temperature on the cracking mechanisms. Both areas are touched upon lightly in this research; they remain to be followed up in the future.

4. PUBLICATIONS AND PRESENTATIONS

The following is a list of publications and presentations that resulted from this research program. Oral presentations (without publishing the accompanying paper) listed here include only those delivered at technical conferences; they do not include the numerous presentations at invited seminars by the participants in the research. Most of the papers listed here have, at various times, been submitted to AFOSR in our routine reporting; all may be requested by writing to the Principal Investigator of this research.

A. AFOSR Technical Reports:

[A-1] "A comprehensive study of matrix fracture mechanisms in fiber-reinforced ceramic matrix composites," AFOSR Annual Technical Report, March 1991.

[A-2] "A comprehensive study of matrix fracture mechanisms in fiber-reinforced ceramic matrix composites," AFOSR Annual Technical Report, March 1992.

[A-3] "A comprehensive study of matrix fracture mechanisms in fiber-reinforced ceramic matrix composites," AFOSR Final Technical Report, June 1993.

B Ph. D. Dissertations:

[B-1] "Matrix cracking initiation stresses in fiber-reinforced ceramic matrix composites," by P. Kangutkar, Drexel University, Dec. 1991 (advisor: M. Barsoum).

[B-2] "On a model approach for damages in ceramic matrix composites," by X.-G. Huang, Drexel University, Feb. 1992 (advisor: A. S. D. Wang).

[B-3] "Mechanics of the single fiber pullout problem with several interface conditions," by Kishore Pochiraju, Feb. 1993 (advisor A. S. D. Wang/A. W. Lau)

C Journal Papers, published:

[C-1] "Effects of temperature on interface bonding of SiC-Glass single-fiber specimens", by H. M. Chou, M. Barsoum and M. J. Koczak. Jour. Matls. Sci. vol. 26, 1991. pp. 1216-22.

[C-2] "Effect of oxidation on single fiber pullout interfacial shear stresses in a SiC-Borosilicate glass system", by I. C. Tung, M. Barsoum and H. M. Chou. Jour. Am. Cer. Soc. vol. 74, 1991. pp. 2693-96.

[C-3] "Matrix crack initiation in ceramic matrix composites: Part 1 Experiment and test results", by M. Barsoum, P. Kangutkar and A. S. D. Wang. Composites Sci. & Tech. vol. 43, 1992. pp.257-269.

[C-4] "Matrix crack initiation in ceramic matrix composites: Part 2 Models and simulation results", by A. S. D. Wang, M. Barsoum and X. G. Huang. Composites Sci. & Tech. vol. 43, 1992. pp.271-282.

[C-5] "Thermal expansion of silicon carbide monofilaments and silicon carbide borosilicate

composites," by A. Elkind, M. Barsoum and P. Kangutkar. J. Am. Ceramic Soc. Vol. 75, 1992. pp.2871-73.

D. Journal Papers, accepted:

[D-1] "On matrix cracking in fiber reinforced ceramics" Jour. Mechanics and Physics of Solids, by I. C. Chiang, A. S. D. Wang and T. W. Chou (accepted);

[D-2] "Modeling of crack deflection in whisker-reinforced ceramic matrix composites," by I. C. Chiang, T. W. Chou and A. S. D. Wang, Jour. Composite Materials, (accepted);

[D-3] "Matrix Cracking Initiation stresses in Uniaxially Fiber Reinforced Ceramic Composites: Part 1. Model and Effects of Matrices," by M. Barsoum, P. Kangutkar and A. S. D. Wang, Journ. Amer. Ceramic Soc. (accepted).

[D-4] "A local-global matching method for the single fiber pullout problem with perfectly bonded interface," by K. Pochiraju, A. C. W. Lau and A. S. D. Wang, J. Computational Mechanics (accepted).

[D-5] "Grain growth and mechanical properties degradation of SiC monofilaments at high temperatures," by A. Elkind and M. Barsoum, J. Am. Ceramic Soc. (accepted).

[D-6] "Residual stresses in SiC/glass composites," by A. Elkind and M. Barsoum, J. Am. Cer. Soc. (accepted).

E. Papers in Conference Proceedings, published:

[E-1] " The Fiber Pull-out Problem: Matching of Singular and Complete Stress Fields," by P. V. Kishore, A. C. W. Lau and A. S. D. Wang, 6th Technical Conference, Amer. Soc. Composites, 1991. pp.1054-63

[E-2] "In-Situ Observation of Damage Initiation and Evolution in Unidirectional Fiber Reinforced Ceramic Matrix Composites," by P. Kangutkar, M. Barsoum and A. S. D. Wang, 1st Canadian Inter. Composites Conference (CANCOM '91), Montreal, Canada, Sept. 1991. 2E6-1

[E-3] "Fracture initiation in ceramic matrix composites," by A. S. D. Wang, Proc. 2nd Int. Conf. Composite Mat. & Struct., Beijing, China. Aug. 1992. pp.793-799.

[E-4] "A probabilistic-mechanistic approach for damage mechanics in fiber-reinforced composites," Keynote Lecture, Proc. 2nd Int. Conf. Composite Mat. & Struct., Beijing, China. Aug. 1992. pp. 1-18.

[E-5] "On fiber-matrix interfaces with frictional shear," by P. V. Kishore, A. C. Lau and A. S. D. Wang, Proc. 7th ACS Technical Meeting, Technomic Pub. 1992. pp. 827-836

F. Papers Presented to Conferences (without a Proceeding):

[F-1] "Matrix cracking in fiber-reinforced ceramic matrix composites", P. Kangutkar and M. Barsoum, 93rd Annual Meetings, Am. Cer. Soc. Cincinnati, OH, April-May 1991.

[F-2] "Effects of temperature and environment on the interfacial shear strength between SiC and glass", I. C. Tung, M. Barsoum and H. M. Chou, 93rd Annual Meetings, Am.

Cer. Soc. Cincinnati, OH, April-May 1991.

[F-3] "Mechanics of matrix damages in ceramic matrix composites", A. S. D. Wang and Michel W. Barsoum, 2nd. USA-USSR Symposium on Mechanics of Composite Materials, Albany, NY. Oct. 1991.

[F-4] "Thermal expansion of SiC monofilaments and SiC-glass composites," by A. Elkind, M Barsoum and P. Kangutkar, to 94th Annual Meet. Amer. Ceramic Soc. April, 1992.

[F-5] "The single fiber pullout problem with perfectly bonded interface," Int. Conf. Computational Engineering Science (ICES-92), Hongkong, 1992.

G. Paper Submitted to Technical Conferences to be Held in 1993:

[G-1] "Simulation of fiber pullout with frictional interface in CMC," by K. Pochiraju, A. S. D. Wang and A. C. W. Lau, 8th ACS Technical Meeting, Cleveland, OH. Oct. 1993.

H. Paper Just Completed:

[H-1] " Pullout Experiment of SCS6 and SCS9 Fibers in Borosilicate Glass Matrix," by J. C. Gong and T. M. Tan, Drexel University, 1992.

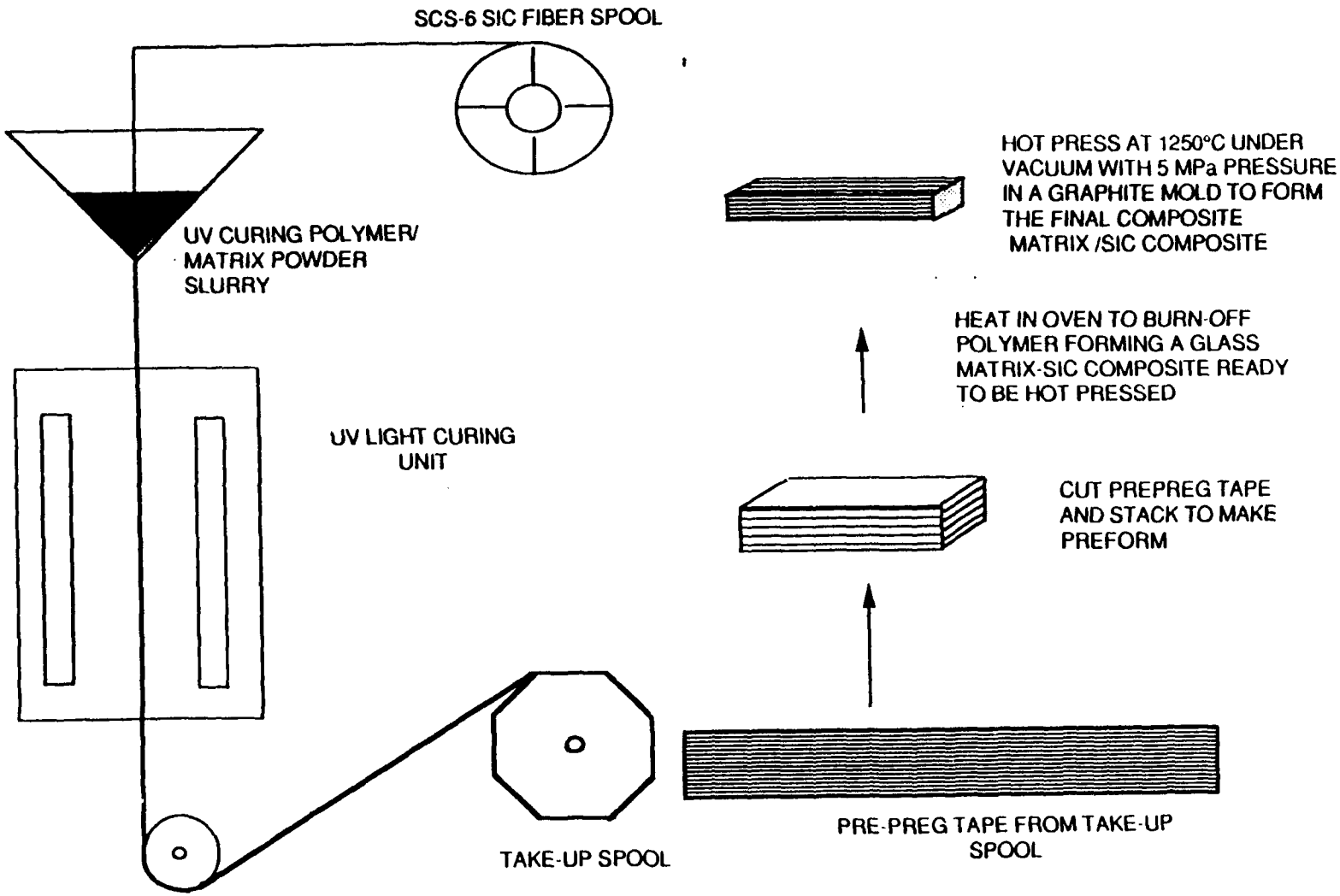

Fig. 1. Schematic flaw-chart for composite fabrication

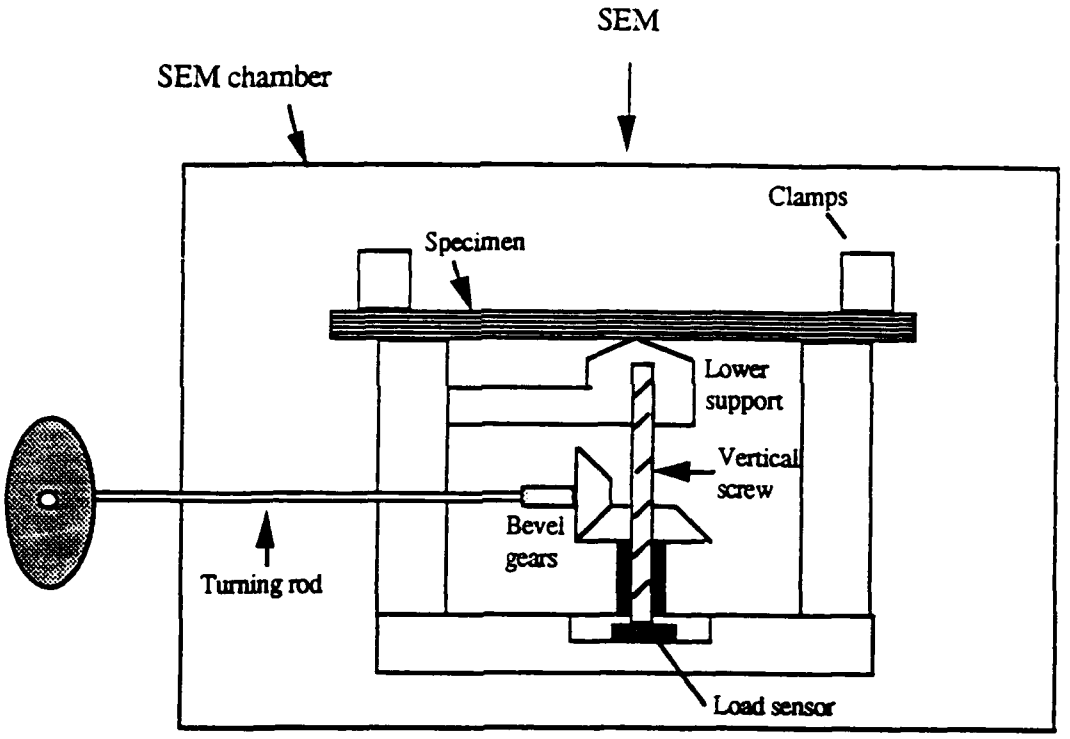

Fig. 2 Schematics of the SEM 3-point bend test fixture with specimen.

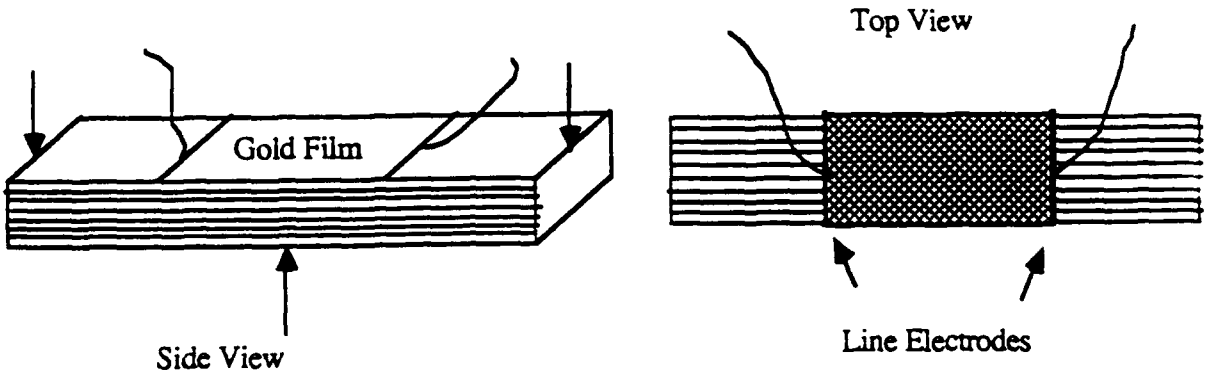

Fig. 3. Schematics of the test specimen with a gold-film for surace crack detection.

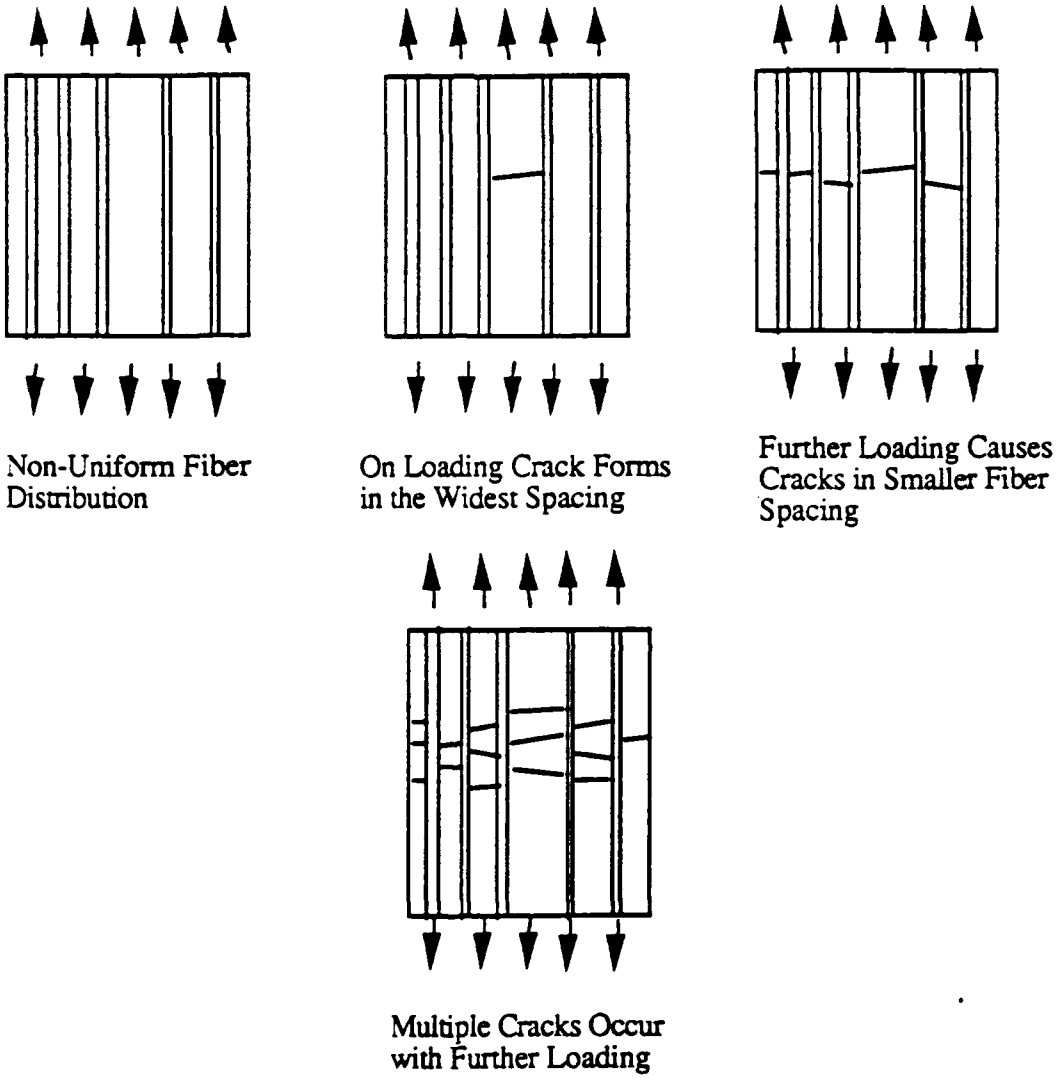

Fig. 4. Schematics of the matrix microcracking sequence as seen in the SEM.

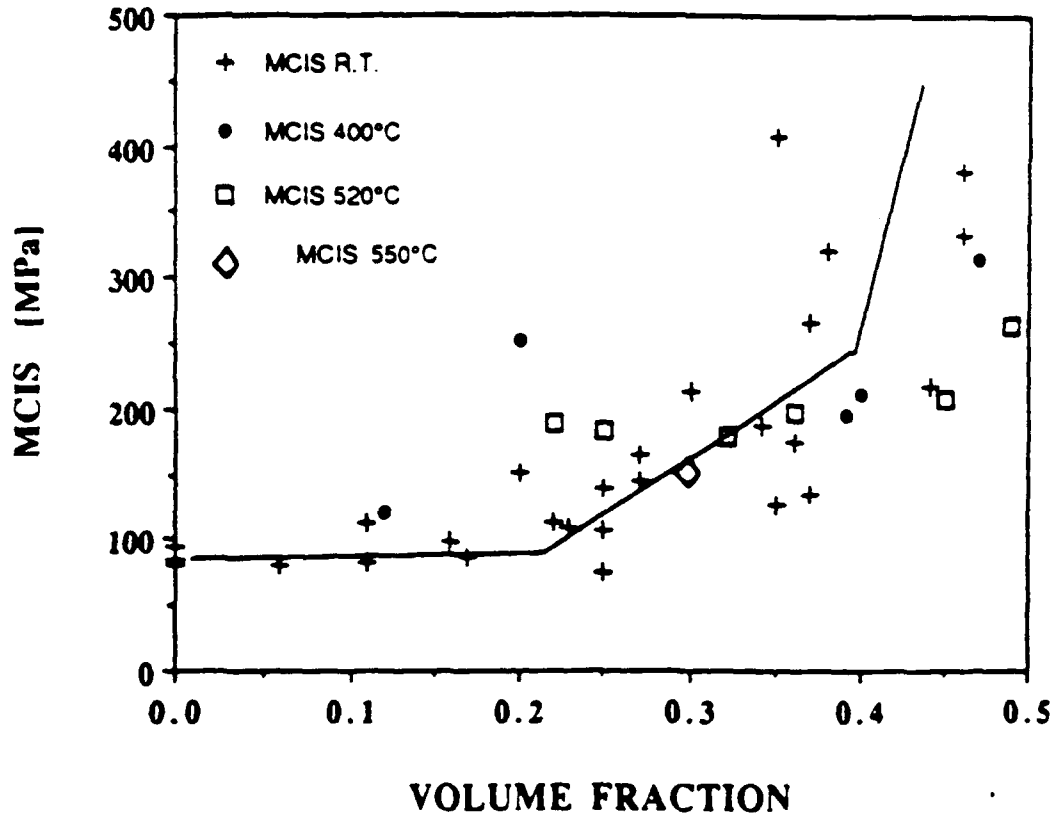

Fig. 5. A collection and presentation of the matrix cracking initiation data (SCS-6/7740).

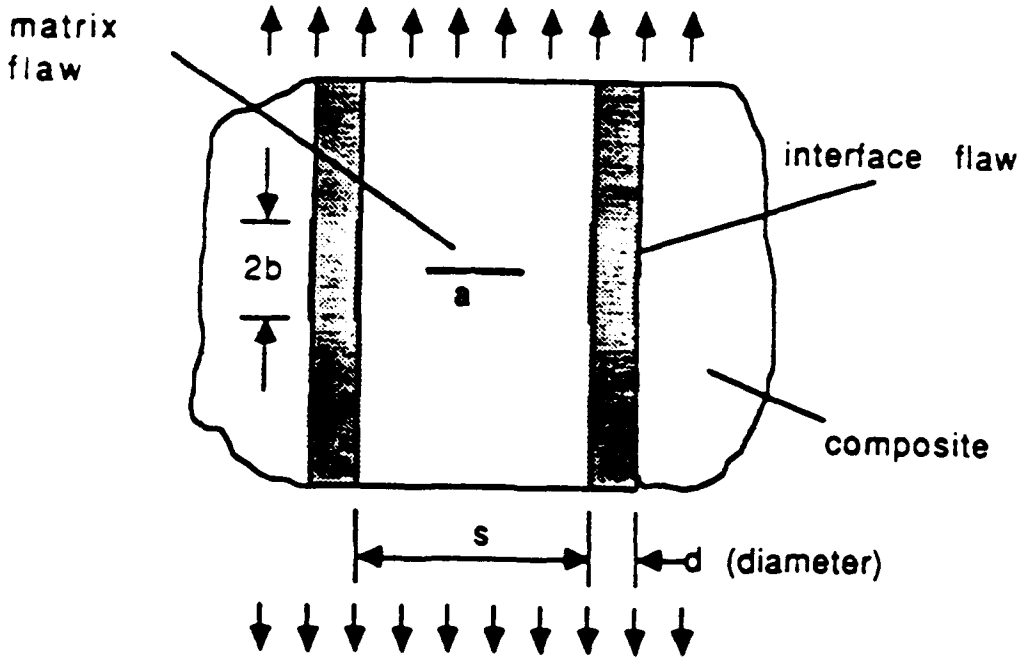

Parameters:

constituents elastic moduli - $(E, \nu)_{f,m}$

strength properties - γ_m

thermal/processing - $\Delta\alpha$, ΔT

microstructure - a probabilistic local unit-cell:

- V_f, R (fiber radius), s (fiber spacing)
- microflaws in matrix and interface (a, b)

Fig. 6. The unit-cell model for matrix microcrack simulation

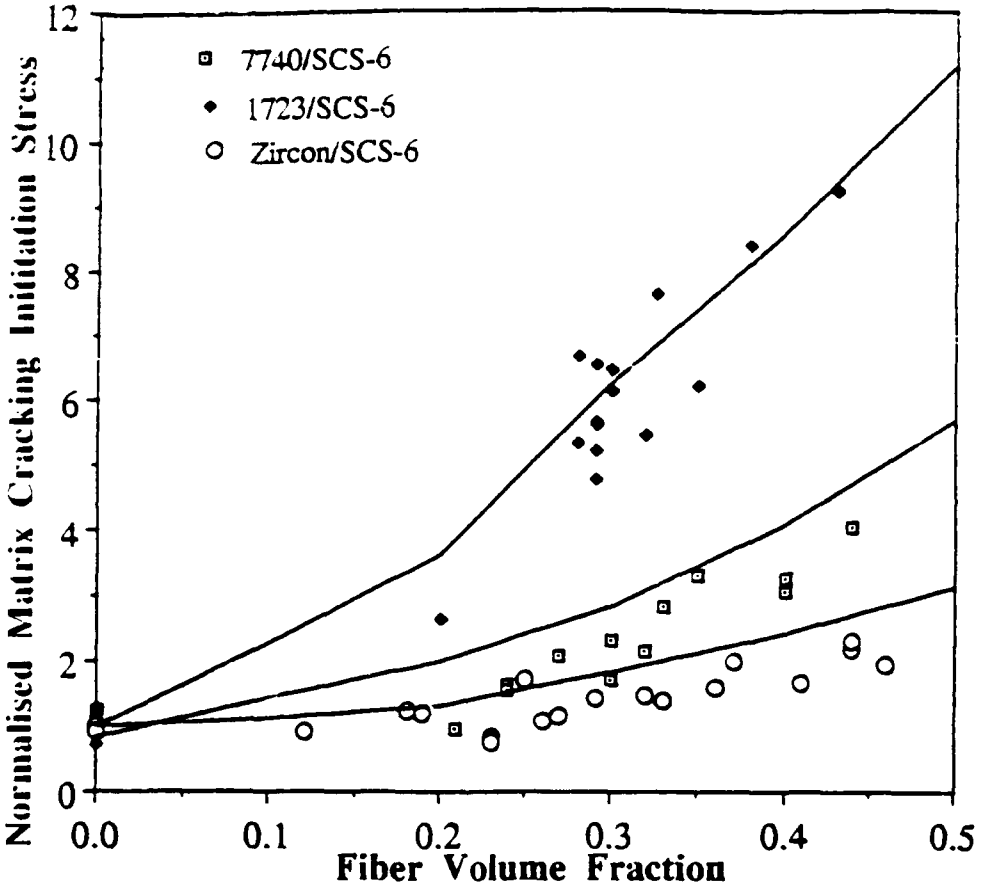

Fig. 7. Comparison between the predicted and experiment MCIS results

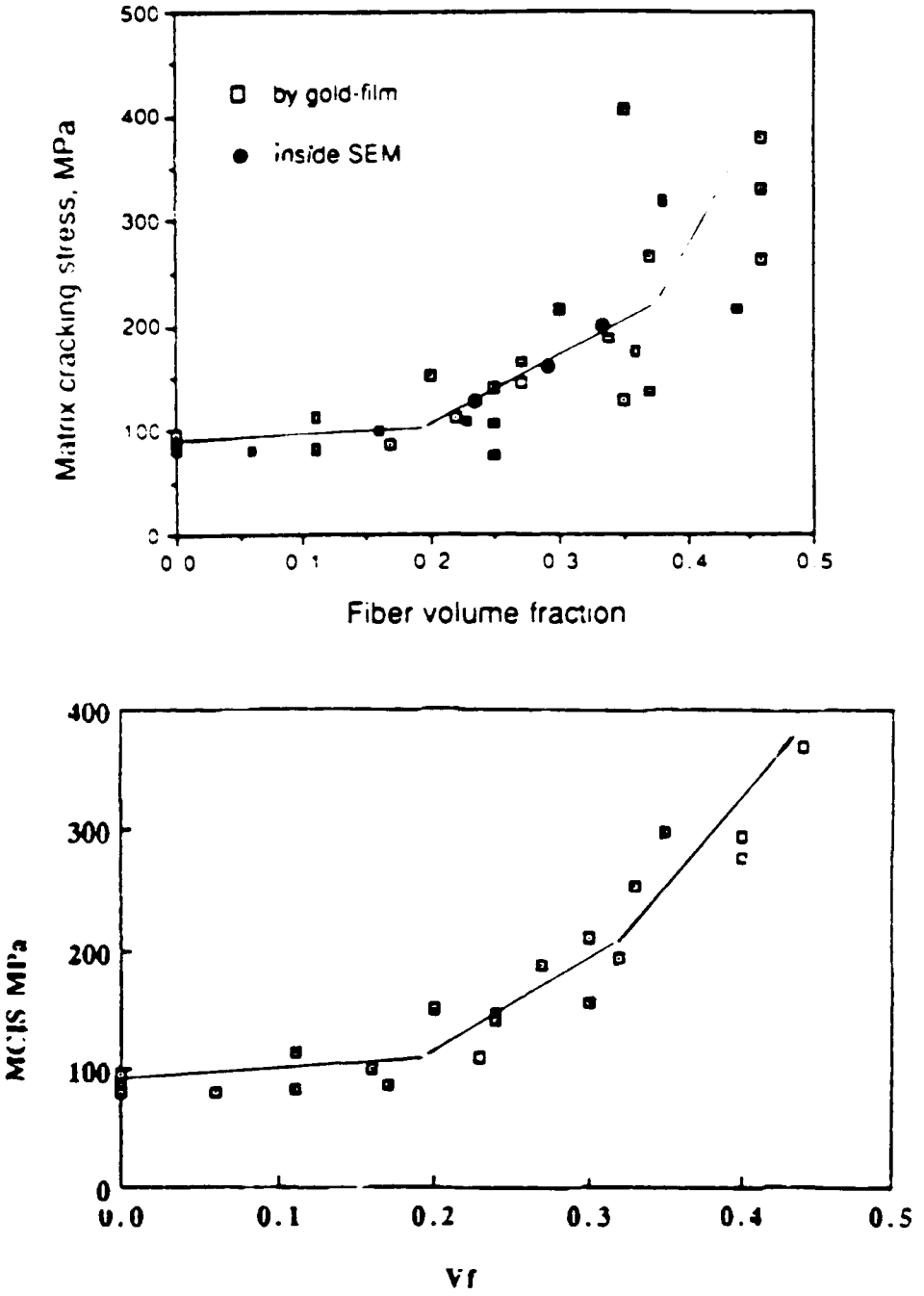

Fig. 8. Effect of specimen polishing on MCIS: (above) unpolished (below) polished

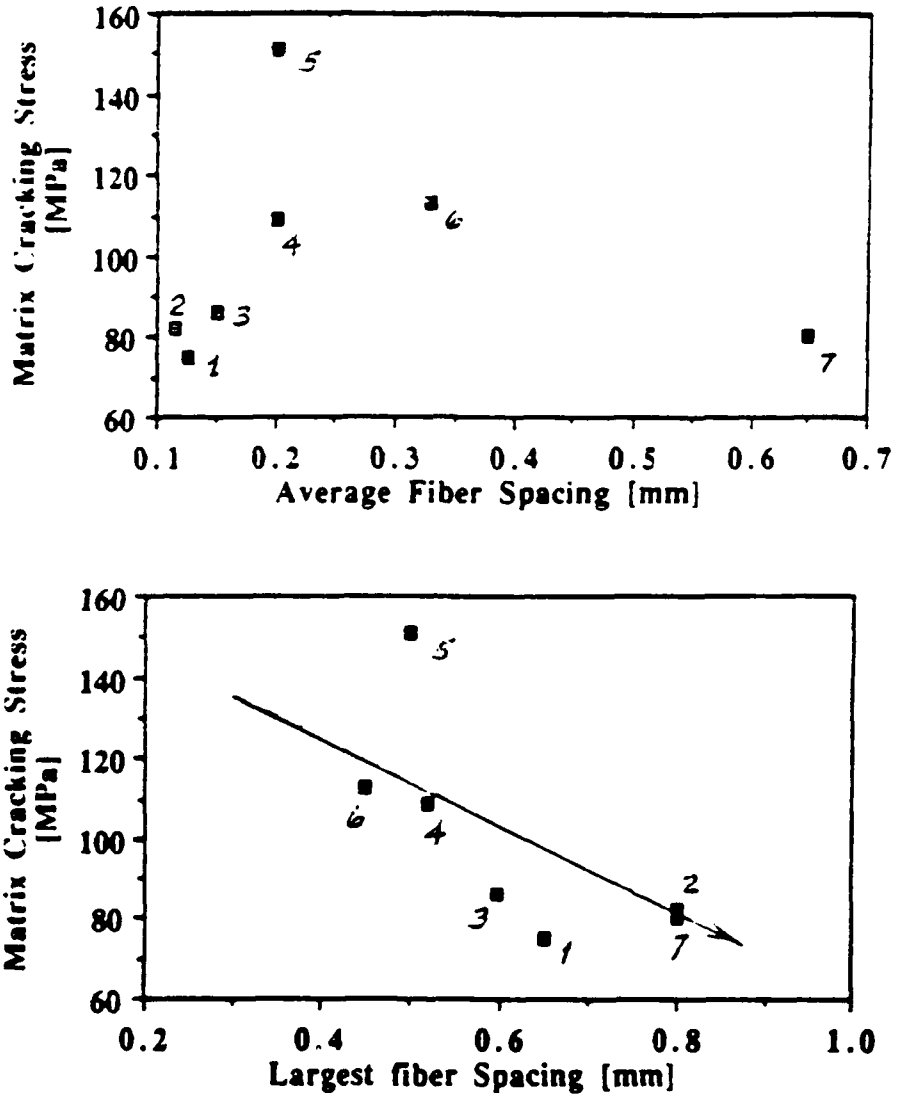

Fig. 9. Effect of fiber spacing on MCIS. (above) MCIS plotted vs. average spacing; (below) MCIS plotted vs. spacing in which crack occrred

R = 70 μm for SCS-6

R = 8 μm for Nicalon

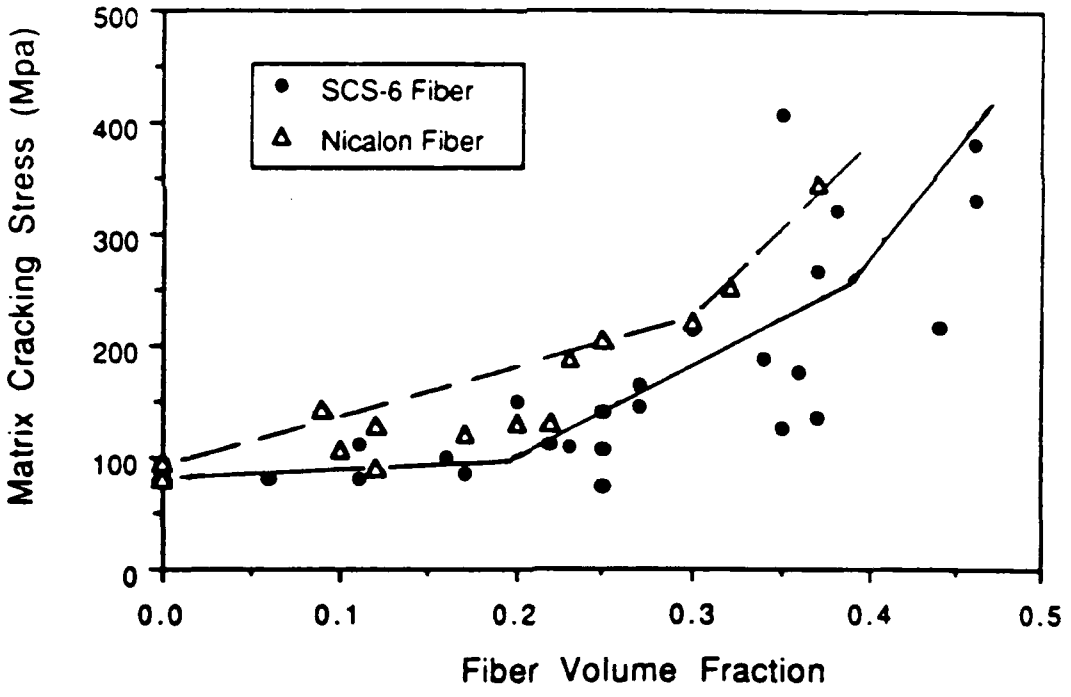

Fig. 10. Effect of fiber diameter on MCIS. SCS-6 vs. Nicalon

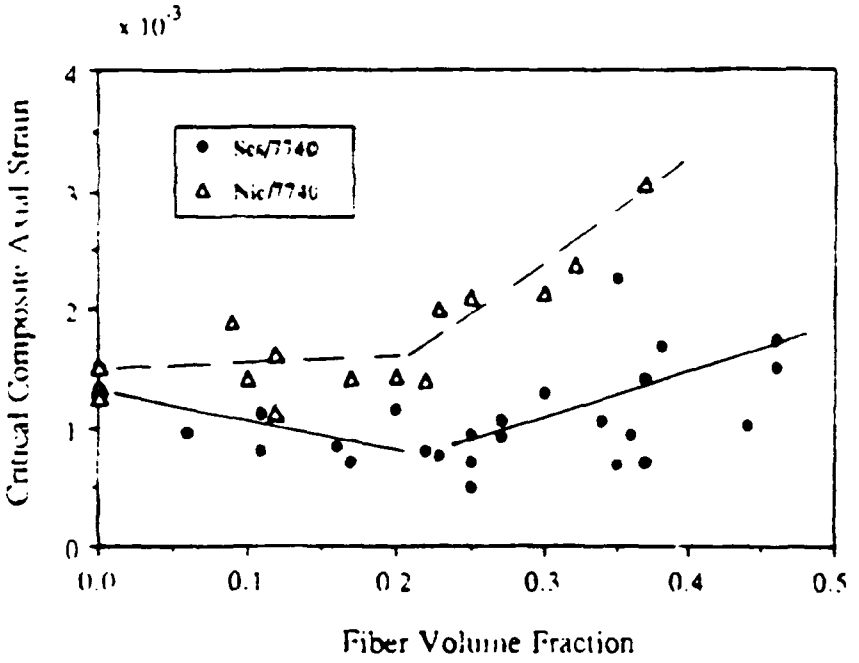

Fig. 11. Effect of fiber diameter on matrix cracking strain. SCS-6 vs. Nicalon

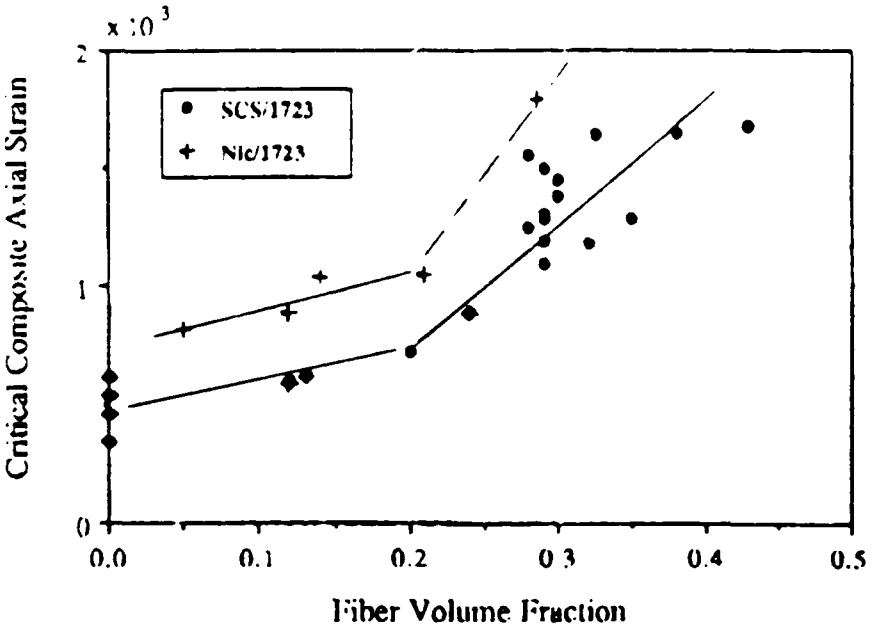

Fig. 12. Effect of fiber diameter on matrix cracking strain. SCS-6 vs. Nicalon with 1723

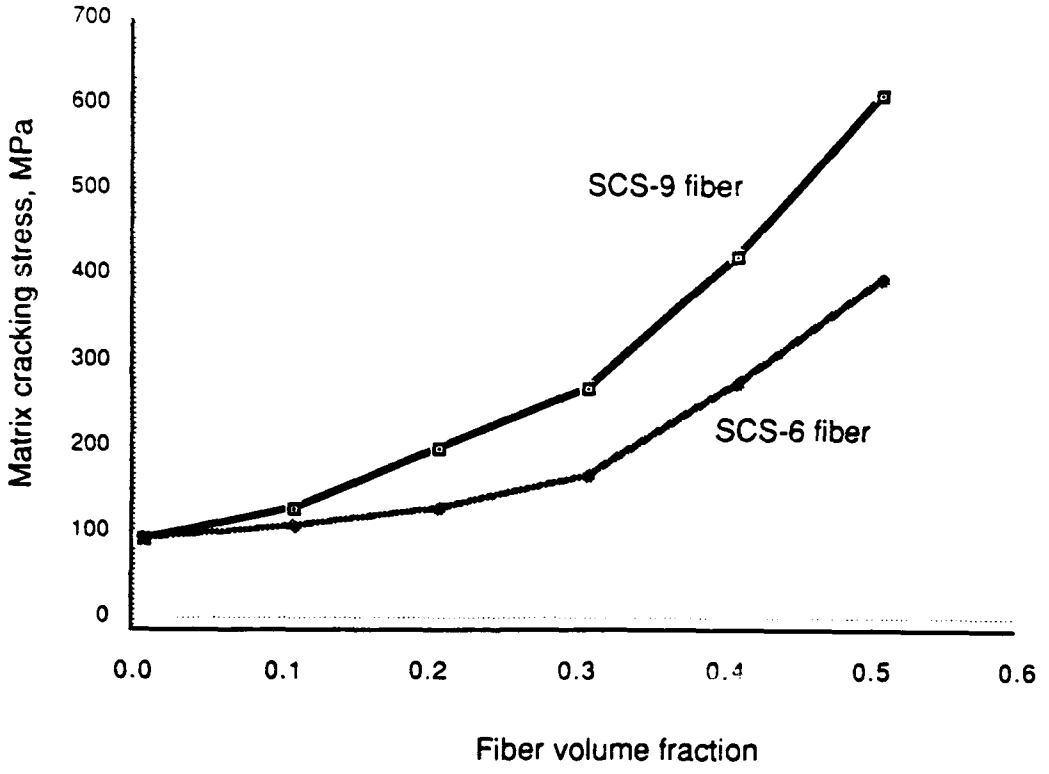

Fig. 13. Effect of fiber diameter on MCIS as predicted by model.
SCS-6 and SCS-9 with 7740

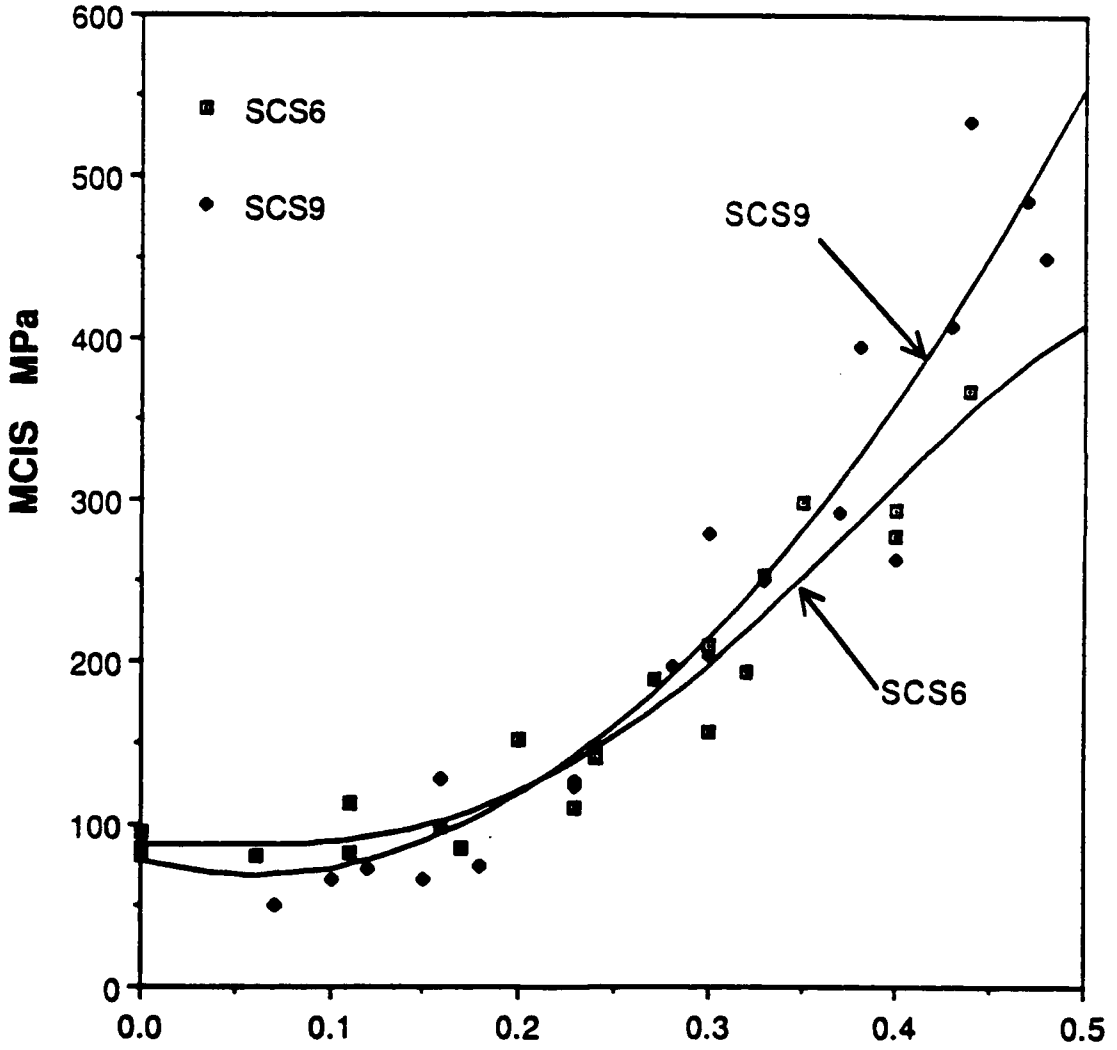

Fig. 14. Effect of fiber diameter on MCIS as illustrated by test results. SCS-6 and SCS-9 with 7740

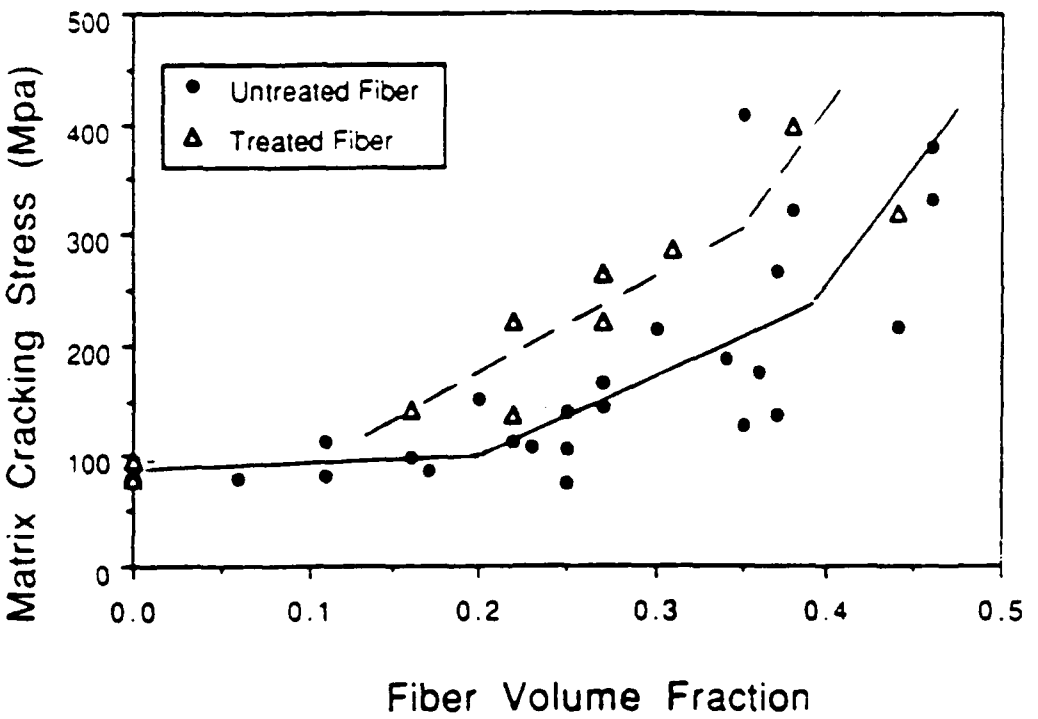

Fig. 15. Effect of fiber surface treatment on MSIC.
SCS-6 with 7740

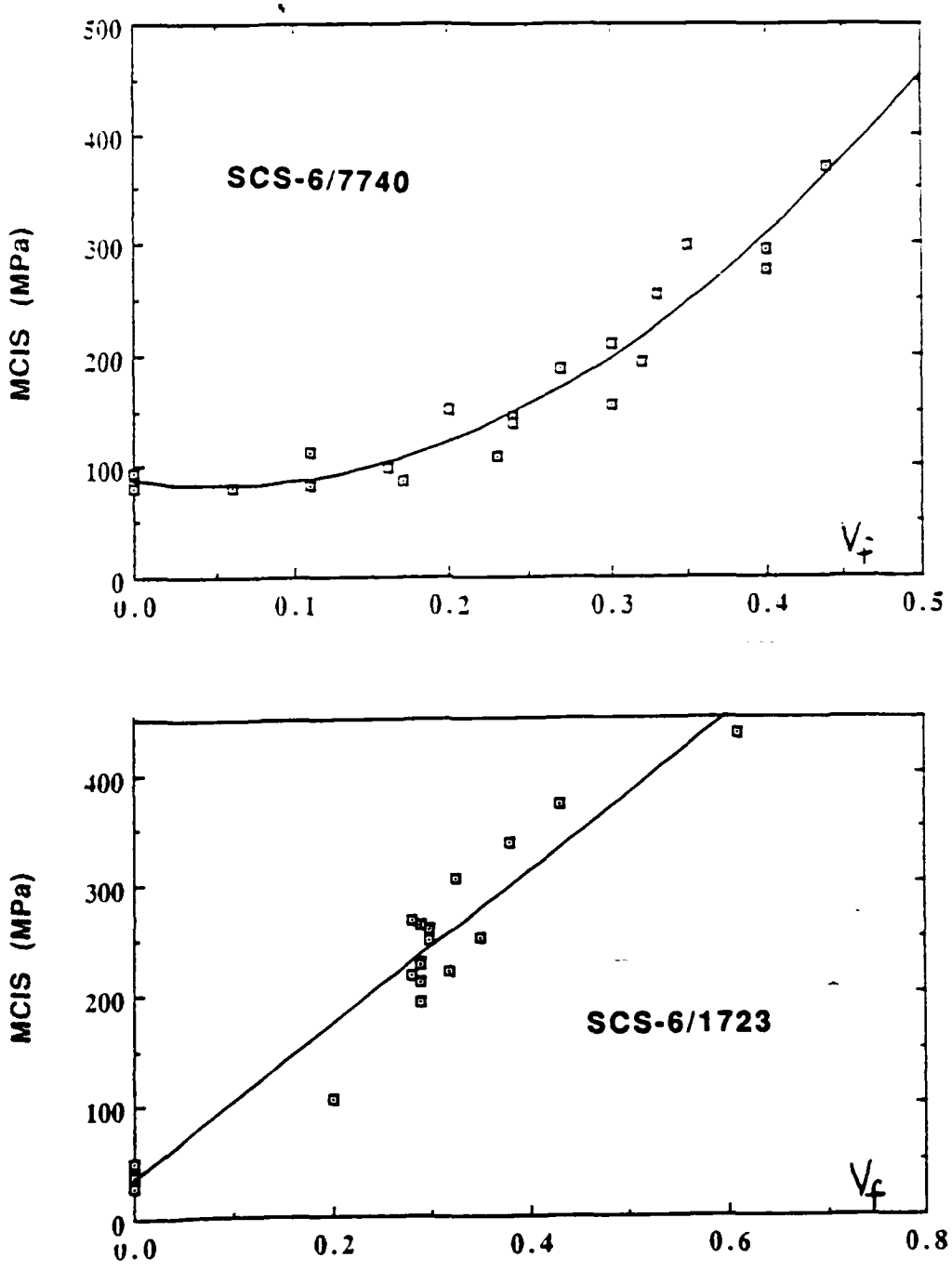

Fig. 16. Effect of matrix flaw size on MSIC.
SCS-6 with 7740 and 1723

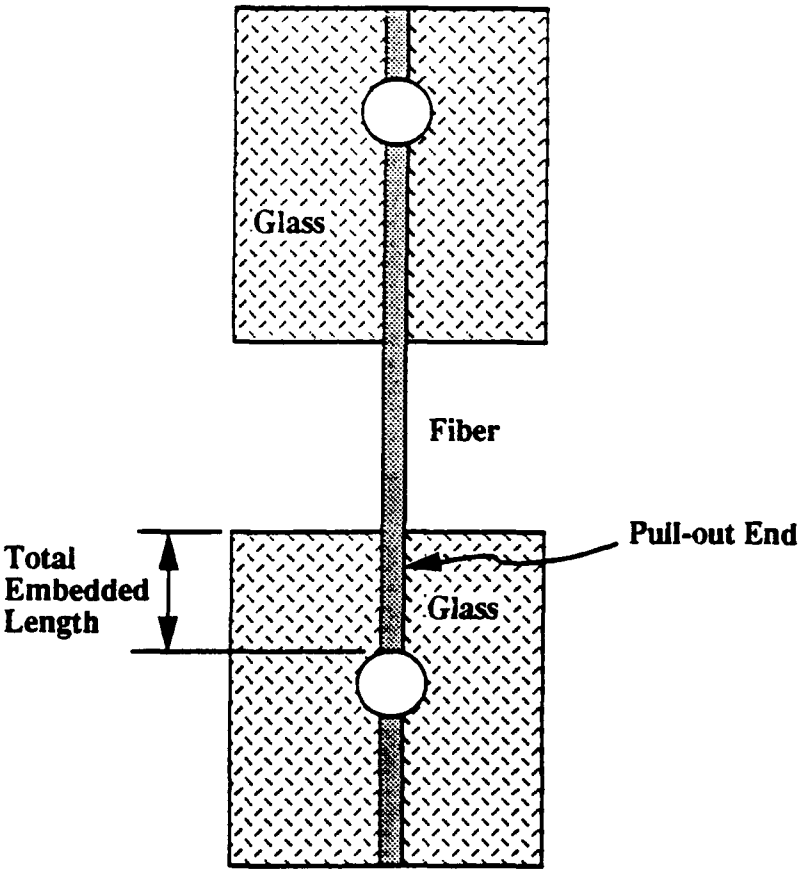

Fig. 17. Schematics for the single fiber pullout test

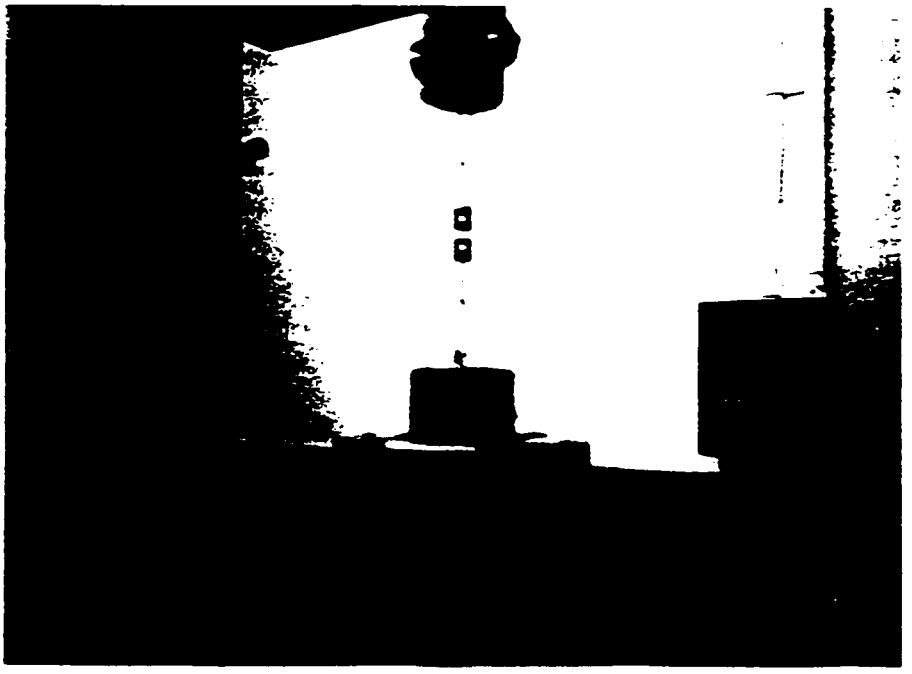

Fig. 18. Machine set-up for the single fiber pullout test

APPENDIX

The following papers are appended to this report for purpose of reference (all papers listed above may be furnished upon request):

1. "A local-global matching method for the single fiber pullout problem with perfectly bonded interface," by K. Pochiraju, A. C. W. Lau and A. S. D. Wang, J. Computational Mechanics (accepted).

2. "Thermal expansion of silicon carbide monofilaments and silicon carbide borosilicate composites," by A. Elkind, M. Barsoum and P. Kangutkar, J. Am. Ceramic Soc. Vol. 75, 1992. pp.2871-73.

Submitted to Computational Mechanics, 5/93

A Local-Global Matching Method for the Single Fiber Pullout Problem with Perfectly Bonded Interface

Kishore V. Pochiraju[†], Alan C. W. Lau[*] [§] and Albert S. D. Wang[§]

[†]Center for Composite Materials, 201, CMSL
University of Delaware,
Newark, DE 19716 USA

[*]*Corresponding Author*

[§]Department of Mechanical Engineering and Mechanics
Drexel University,
Philadelphia, PA 19104 USA

ABSTRACT

This paper presents a local-global matching method to effectively solve both the detail spatial structure of the locally singular stress field and the complete global stress distribution in the single fiber pullout model. The main motivation to solve for the locally accentuated stress field is the belief that locally elevated stresses, strains and energy are likely to induce damage formation and growth. The method consists of three components: a local analysis, a global analysis, and proper local-global matching of the local asymptotic field to the global complete stress field. The method is applicable for various fiber-matrix interfacial conditions: perfectly bonded, partially debonded with interfacial crack, or debonded with frictional interfacial sliding. Results presented here are those of perfectly bonded fiber-matrix interface. For this problem, the local stress field is asymptotically singular (unbounded) at the immediate vicinity where the fiber protrudes from the matrix. In the local analysis, use of complex potential and asymptotic expansion shows that when the fiber is stiffer than the matrix the most dominant singular

stresses at the fiber protrusion point are of the form: $\sigma_{ij}(\rho,\theta) = K\,\rho^{\lambda}\tilde{\sigma}_{ij}(\theta)$ where the exponent λ is real-valued and $\lambda < 0$. The local analysis determines the analytic spatial structure of the local field: the radial dependence ρ^{λ} and angular variations of the stresses $\tilde{\sigma}_{ij}(\theta)$. The actual magnitude of the local stress field is scaled by the amplitude factor K which depends upon externally applied load and overall boundary conditions. The global analysis, performed by a finite element model, can be subjected to arbitrary fiber-pulling load and/or thermal load. The local-global matching method is based on matching the angular variation of the local asymptotic field to the finite-element computed full-field stresses to determine K. Several monitoring parameters are developed to quantify the quality of the matching. In many composite systems, there are two singular terms in the local field: $\sigma_{ij} = K_1\rho^{\lambda_1}\tilde{\sigma}^1_{ij}(\lambda;\theta) + K_2\rho^{\lambda_2}\tilde{\sigma}^2_{ij}(\lambda;\theta)$. Consequently, local-global matching procedures for one-term matching and two-term matching are developed in this paper. Then, the method is generalized to determine complex-valued K for stress field having complex-valued λ. It is pointed out that the local-global matching method also applies to problems with material nonlinearity. Numerical examples are presented to illustrate germane features of the method.

1 Introduction

The load transfer between fiber and matrix is of importance to the evolution of damage in composites. In particular, the fiber-matrix load transfer during fiber pullout, the interfacial damage mechanisms, the interface strength, and the overall toughness of brittle matrix composites are intimately related (Kerans, Hay, Pagano and Parthasarathy (1989) and Evans and Marshall (1989)). The pulling-out (or pushing-in) of a single fiber embedded in a concentric cylinder of matrix has been used to study the fiber-matrix load transfer and to characterize the fiber-matrix interfacial strength. For the single fiber pullout model, this study presents an effective method to solve for not just the overall

stress distribution but also the detail analytical form of accentuated local stresses at geometric and material discontinuity where damage is most likely to develop.

The problem of a single fiber embedded in a matrix was examined by Greszczuk (1969), McCartney (1989), Hutchinson and Jenson (1990) and Kurtz and Pagano (1991), among others. In these solutions, the emphasis was not on the detail stress distribution at the local regions where damage may initiate or propagate, hence the exact nature of the local accentuated stress field near the fiber protrusion point (one of the local regions) was not rigorously determined. In our work, closed-form expressions were determined to solve for the radial and angular variations of locally singular stresses for the single fiber pullout problem. Unlike crack-tip solutions, in this problem two singular stress terms with different radial dependence are found for many fiber and matrix combinations. This paper focuses on developments relevant to the local-global matching method. Other details on the analyses and characteristics of the stress fields are presented in Pochiraju (1993) and Pochiraju, Lau and Wang (1992, 1993).

The general approach of solution involves three essential steps. The first step concerns the detail form of local stress field in the singular region. In the local analysis, a power-type asymptotic eigenvalue expansion of the Muskhelishvili-Kolosov stress potential functions is utilized to solve for the singular local stress field. The local analysis determines the exponent of the singularity and the associated spatial variation of the dominant stress field. The second step is a global analysis using finite element method to determine the complete stress distribution over the entire domain corresponding to any specific mechanical and/or thermal loading and boundary constraints. In the third step, a local-global matching method based on the angular variation of stresses is performed. A zone is determined near the singular point in which the angular variations of the finite element computed stresses match perfectly with those of the local asymptotic singular field. The perfect match determines the amplitude factor

K of the local singular stress field, thus giving completely the analytic local stress distribution.

This local-global matching method is versatile and can be used to solve the local singular stress fields in a variety of problems. This analytical-computational method is easily applicable for arbitary mechanical and/or thermal loading, and for a variety of fiber-matrix interfacial conditions. Results of applying the local-global matching method to frictional sliding and partially cracked fiber-matrix interface problems are reported in Pochiraju (1993). With minor modification, the local-global matching method presented here is also applicable to material nonlinear problems. One of the authors (Lau) has applied local-global matching to power-law creeping alloys with sliding grains (Lau, Argon and McClintock (1983)) and power-law plastically deforming metal matrix composites (Tan, Lau and Rahman (1989)). The theoretical basis and recent developments of the local-global matching method are presented in Sections 3, 4 and 5. As a starting point, Section 2 summarizes the determination of local singular stress field in the fiber pullout problem.

2 Local Analysis

The physical model considered is shown in Figure 1. A single fiber of radius R_o is embedded in a concentric cylinder of matrix material of outer radius $\frac{R_o}{\sqrt{V_f}}$, where V_f is the fiber volume fraction of the composite material. A global cylindrical coordinate system $\{R, Z, \phi\}$, with Z along the axis of the fiber is adopted to describe the overall geometry. The view at right shows a cross-section of the meridian plane A-A at any specific ϕ value. As shown in the cross-sectional view A-A, the embedded length of the fiber is denoted by t, and its protruded length is assumed to be $10R_o$ or longer. To eliminate rigid body motion, let the $Z = t$ plane of the matrix cylinder be constrained not to move in the Z-direction. If the protruded fiber is pulled outward (or pushed inward), and/or the composite is subjected to a thermal load ΔT, load transfer from the fiber to the

matrix takes place through their mutual interface at $R = R_o$. Since the geometry and loading in this model has global axisymmetry, we only need to solve for the solution in the meridian plane of any arbitrary ϕ.

The point where the fiber protrudes from (or enters into) the matrix is labeled as O. The fiber protrusion point O is a site of geometric and material discontinuity where local accentuation of stresses and strains occur. In the local analysis, our goal is to determine the detail spatial structure of the stress field at the immediate vicinity of O. The motivation to solve for the locally accentuated stress/strain field is the belief that locally elevated stresses, strains and energy are likely to induce damage formation and growth. To solve for this locally accentuated (in fact, singular) stress field, it is convenient to define a local coordinate system $\{\rho, \theta\}$ with origin at point O.

In axisymmetric problems, at locations where the length scale is much smaller than the local curvature, the dominant terms of the governing equation in the axisymmetric model are identical to the plane strain governing equation (see equations (11) and (12) of Zak (1964) and section 3.4 of Atkinson, Avila, Betz and Smelser (1982)). Within a region $\frac{\rho}{R_o} << 1$ around the fiber protrusion point O, the axisymmetric local stress field can be solved by treating the material as locally under plane strain condition, and use analytic methods originally developed for plane strain governing equations.

In the local analysis, we applied Muskhelishvili- Kolosov complex potential theory to both the fiber and matrix domains (see Section A-A, Figure 1). In each domain, the components of stresses are expressed in terms of the spatial derivatives of two complex potential functions, $\Omega(z)$ and $\omega(z)$ (England (1971), pp. 53-55). The fiber-matrix interfacial conditions connect the solutions of the two domains together.

A power-type solution is sought using Taylor series expansion of the complex potential functions at the immediate vicinity of the fiber protrusion point O:

$$\Omega(z) = \sum_{n=1}^{\infty}\left(A_n z^{S_n} + A_n^* z^{\overline{S_n}}\right)$$
$$\omega(z) = \sum_{n=1}^{\infty}\left(B_n z^{S_n} + B_n^* z^{\overline{S_n}}\right) \qquad (1)$$

The normal and shear stress components and the displacement components with a single term (n=1, and S_1=S) expansion in (1) are:

$$\begin{aligned}\tau_\theta(\rho,\theta) &= \sigma_{\theta\theta}(\rho,\theta) - i\sigma_{\rho\theta}(\rho,\theta)\\ &= S\rho^{S-1}\left(Ae^{i(S-1)\theta} + \overline{A^*}Se^{-i(S-1)\theta} + \overline{B^*}e^{-i(S+1)\theta}\right) + \bar{S}\rho^{\bar{S}-1}\left(A^*e^{i(\bar{S}-1)\theta} + \overline{A}\bar{S}e^{-i(\bar{S}-1)\theta} + \overline{B}e^{-i(\bar{S}+1)\theta}\right)\\ &= S\rho^{S-1}\tilde{\sigma}_1(\theta) + \bar{S}\rho^{\bar{S}-1}\tilde{\sigma}_2(\theta)\end{aligned} \qquad (2a)$$

$$\begin{aligned}GU(\rho,\theta) &= G\left(u_\theta(\rho,\theta) + iu_\rho(\rho,\theta)\right)\\ &= \rho^S\left(A\kappa e^{i(S-1)\theta} - \overline{A^*}Se^{-i(S-1)\theta} - \overline{B^*}e^{-i(S+1)\theta}\right) + \rho^{\bar{S}}\left(A^*\kappa e^{i(\bar{S}-1)\theta} - \overline{A}\bar{S}e^{-i(\bar{S}-1)\theta} - \overline{B}e^{-i(\bar{S}+1)\theta}\right)\end{aligned} \qquad (2b)$$

Denoting λ =S-1, for a single term in the expansion of (1):

$$\sigma_{ij}(\rho,\theta) \propto \rho^\lambda \tilde{\sigma}_{ij}(\theta) \qquad (3)$$

Equation (3) establishes the spatial characteristics of the stress fields in the local regions. The stresses in the local region have a power-type dependence on the radial coordinate ρ. When $\lambda < 0$, the local stresses have a power-type singularity. In our analysis, both real-valued and complex-value stress singularities are allowed (λ can be real or complex).

The complex-valued constants A, B, A^*, B^*, their conjugates, and possibly complex-valued λ are determined using the local boundary conditions and fiber-matrix interfacial conditions (see Section A-A, Figure 1). For a perfectly bonded fiber-matrix interface, the stress components $\sigma_{\theta\theta}$ and $\sigma_{\rho\theta}$, and the displacement components u_θ and u_ρ , are continuous across the fiber-matrix interface. The other surfaces of the matrix and the protruding fiber are traction free. Denoting quantities in the fiber domain with a superscript *f* , and quantities in the matrix domain with superscript *m*, the local interfacial and boundary conditions can be expressed as:

Fiber - matrix interface conditions:

$$\text{At } \theta = 0: \qquad \tau_\theta^f(\theta=0) - \tau_\theta^m(\theta=0) = 0$$
$$U_\theta^f(\theta=0) - U_\theta^m(\theta=0) = 0$$

Traction free boundary conditions: (4)

$$\text{At } \theta = -\frac{\pi}{2}: \qquad \tau_\theta^m(\theta=-\frac{\pi}{2}) = 0$$
$$\text{At } \theta = \pi: \qquad \tau_\theta^f(\theta=\pi) = 0$$

Substituting (2) in (4), four homogenous equations with complex-valued coefficients (eight real-valued equations) can be obtained. These four equations along with their four complex conjugates form the system of governing equations:

$$[C]\{\bar{X}\} = \{0\} \tag{5}$$

where $$\{\bar{X}\}^T = \left\{A_f,\ \bar{A}_f^*,\ B_f,\ \bar{B}_f^*,\ A_m,\ \bar{A}_m^*,\ B_m,\ \bar{B}_m^*\right\} \tag{6}$$

In this eigenvalue problem, nontrivial solutions exists when the determinant of $[C]$ vanishes. The determinant of $[C]$ has the analytically form (Pochiraju (1993)):

$$\begin{aligned} D(\alpha,\beta;S) = {} & (\beta^2-1)\cos(3S\pi) + \left\{4S^2(\beta-\alpha)(\beta+1) - 2(\beta^2-\alpha)\right\}\cos(2S\pi) \\ & -(\alpha^2+\beta^2+2\alpha)\cos(S\pi) - 2S^2\left\{(\alpha-\beta)^2+(\beta+1)^2\right\} + 2\beta^2+\alpha^2+1 \\ = {} & 0 \end{aligned} \tag{7}$$

In the above equation α and β are the Dundurs parameters (Dundurs (1969)) :

$$\alpha = \frac{\tau(\kappa_f+1)-(\kappa_m+1)}{\tau(\kappa_f+1)+(\kappa_m+1)} \quad , \quad \beta = \frac{\tau(\kappa_f-1)-(\kappa_m-1)}{\tau(\kappa_f+1)+(\kappa_m+1)} \tag{8}$$

in which $\tau = \frac{G_m}{G_f}$, $\kappa_f = 3-4\nu_f$, $\kappa_m = 3-4\nu_m$, G_m and G_f are the shear moduli of the matrix and fiber respectively, and ν_m and ν_f are the Poisson's ratios of the matrix and fiber respectively.

Our interest is on the dominant terms of (7) that give rise to locally accentuated stresses. Among the many eigenvalues S_n of (7), the ones in the range of $0 < \mathrm{Re}(S_n) < 1$ produce singular stress field but finite strain energy at the fiber protrusion point O. This corresponds to an admissible range of $-1 < \mathrm{Re}(\lambda) < 0$ for λ ($\lambda = S-1$). The zeros of the determinant (7) are searched numerically using modified Powell algorithm (Moré, 1980) with real and imaginary components of λ as independent variables, within the admissible range of $-1 < \mathrm{Re}(\lambda) < 0$.

After the determination of the eigenvalue λ, the eignevector $\overline{X}$ can be determined. Once the complex-valued coefficients A_f, $\overline{A}_f^*$, B_f, $\overline{B}_f^*$, A_m, $\overline{A}_m^*$, B_m, $\overline{B}_m^*$ in $\overline{X}$ are determined, the angular variations $\tilde{\sigma}_1(\theta)$ and $\tilde{\sigma}_2(\theta)$ can be computed using (2). When the fiber is stiffer than the matrix, λ is real-valued. In this case, the rank of the system of governing equations (5) is such that these coefficients can be determined to within one arbitrary real-valued constant. It follows that the stresses are determinable to within one arbitrary amplitude factor K, which scales the magnitude of the stresses. The singular stress field corresponding to λ_1 is

$$\sigma_{ij}^{local}(\rho,\theta) = K_1 \rho^{\lambda_1} \tilde{\sigma}_{ij}^{1}(\lambda_1;\theta) \tag{9}$$

To uniquely define this arbitrary scaling factor K, we set the angular variation of the opening stress at the fiber-matrix interface to be unity , that is $\tilde{\sigma}_{\theta\theta}(\theta = 0) = 1$. The angular variation of the stresses, $\tilde{\sigma}_{ij}^{1}(\lambda_1;\theta)$, are determined by the eigenvalue λ_1 and the coefficients of the eigenvector $\overline{X}$. The magnitude of $\tilde{\sigma}_{ij}^{1}(\lambda_1;\theta)$ are bounded functions of θ. Solution of a typical $\tilde{\sigma}_{ij}^{1}(\lambda_1;\theta)$ from local asymptotic analysis is depicted by the lines in Figure 4.

The eigenvalue λ defines the radial variation of the local stress field, ρ^{λ}. Solutions of λ covering a wide range of fiber-matrix combinations (0.0001< (matrix

elastic modulus /fiber modulus) < 10000) are shown in Figure 2. These results are for Poisson's ratios of $\nu_m = \nu_f = 0.3$. The solution demonstrates that λ is real-valued when the fiber is stiffer than the matrix. For some fiber-matrix combinations, there are ~~be~~ two solutions of λ in the admissible region of $-1 < \lambda < 0$. We denote these two solutions as λ_1 and λ_2, $(\lambda_1 < \lambda_2)$. In these cases there are two singular stress terms in the local analysis, giving rise to a two-term solution :

$$\sigma_{ij}^{local}(\rho,\theta) = K_1\rho^{\lambda_1}\tilde{\sigma}_{ij}^{1}(\lambda;\theta) + K_2\rho^{\lambda_2}\tilde{\sigma}_{ij}^{2}(\lambda;\theta) + \quad \ldots \tag{10}$$

Of these two singular terms, the most negative-valued λ (i.e. λ_1) gives rise to the most singular stress distribution at O.

Figure 3 depicts that, in uncommon ceramic matrix composite materials in which the matrix is very much stiffer than the fiber, λ can be complex-valued. Since complex roots come in conjugate pairs, there are at least two solutions, λ_1 and $\overline{\lambda}_1$, in the admissible range $-1 < Re(\lambda) < 0$. For complex-valued λ, the rank of the system of governing equations (5) is such that for each λ the coefficients in $\overline{X}$ can be determined to within one arbitrarily complex-valued constant. The local singular stress field corresponding to λ_1 and $\overline{\lambda}_1$ have the form:

$$\begin{aligned}
\tau_{\theta}^{local}(\rho,\theta) &= \sigma_{\theta\theta}^{local}(\rho,\theta) - i\sigma_{\rho\theta}^{local}(\rho,\theta) \\
&= K_1\rho^{\lambda_1}\tilde{\sigma}_{\theta}^{A_1}(\lambda_1;\theta) + \overline{K}_1\rho^{\overline{\lambda}_1}\tilde{\sigma}_{\theta}^{B_1}(\overline{\lambda}_1;\theta) \\
\tau_{\rho}^{local}(\rho,\theta) &= \sigma_{\rho\rho}^{local}(\rho,\theta) + i\sigma_{\rho\theta}^{local}(\rho,\theta) \\
&= K_1\rho^{\lambda_1}\tilde{\sigma}_{\theta}^{C_1}(\lambda_1;\theta) + \overline{K}_1\rho^{\overline{\lambda}_1}\tilde{\sigma}_{\theta}^{D_1}(\overline{\lambda}_1;\theta)
\end{aligned} \tag{11}$$

The singular stress field of (9) or (10) is a locally dominant portion of the complete stress distribution. The complete stress field (keeping all higher order terms in (1)) has the form:

$$\sigma_{ij}(\rho,\theta)=\sum_{m=1}^{\infty} K_m \rho^{\lambda_m} \tilde{\sigma}_{ij}^{m}(\lambda_m;\theta) \qquad \text{(when } \lambda \text{ is real)} \qquad (12)$$

and

$$\begin{aligned}
\tau_\theta(\rho,\theta) &= \sigma_{\theta\theta}(\rho,\theta) - i\sigma_{\rho\theta}(\rho,\theta) \\
&= \sum_{m=1}^{\infty} K_m \rho^{\lambda_m} \tilde{\sigma}_{\theta}^{A_m}(\lambda_m;\theta) + \overline{K}_m \rho^{\overline{\lambda}_m} \tilde{\sigma}_{\theta}^{B_m}(\overline{\lambda}_m;\theta) \\
\tau_\rho(\rho,\theta) &= \sigma_{\rho\rho}(\rho,\theta) + i\sigma_{\rho\theta}(\rho,\theta) \\
&= \sum_{m=1}^{\infty} K_m \rho^{\lambda_m} \tilde{\sigma}_{\theta}^{C_m}(\lambda_m;\theta) + \overline{K}_m \rho^{\overline{\lambda}_m} \tilde{\sigma}_{\theta}^{D_m}(\overline{\lambda}_m;\theta)
\end{aligned} \qquad \text{(when } \lambda \text{ is complex)} \qquad (13)$$

The solution of the local analysis is valid for all externally applied loading and remote geometric constraints. Different externally applied loading and remote geometric constraints will only cause difference in the magnitude of the scaling factor K.

The complex potential asymptotic expansion method has been used by several researchers to study stress singularities in wedge geometry (Dempsey and Sinclair (1981), Carpenter (1985), and Iancu, Fett and Munz (1990)). These studies focused on determining the exponent of the stress singularity, λ , at the wedge corner. The amplitude factor K, and hence the actual magnitude of the local field near the wedge corner, were not solved. There are other good methods to analyze bonded wedges, see for example Bogy (1971) and Hein and Erdogan (1971). Many of these methods are particularly suitable for certain class of global loading and boundary conditions, and are not easily extendible to determine the amplitude factor K for arbitrary mechanical and thermal loadings. In the local-global matching method, the amplitude factor K for arbitrary mechanical and thermal loadings for arbitrary global boundary constraints can be easily determined.

3 Global Analysis and Local-global Matching Method

In the global analysis, finite element method (FEM) is used to determine the complete full-field stress distribution. Then, the local-global matching method is used to

link the full-filed stress distribution to the local field to determine the amplitude factor K. The general methodology is illustrated here with one-term matching (matching of the one-term local field (9), $\sigma_{ij} = K_1 \rho^{\lambda_1} \tilde{\sigma}^1_{ij}(\lambda;\theta)$, with finite-element results) to determine K_1. In Section 4, the matching method is extended to two-term matching to determine both K_1 and K_2 for real-valued λ_1 and λ_2. In Section 5, the method is generalized to determine the complex-valued scaling factors for problems with complex-valued λs.

An axisymmetric finite element model with quadratic serendipity (8-noded) quadrilateral elements were used to compute the global full-field solution (Figure 3). Near the fiber-protrusion point O, elements were arranged in concentric rings with the ring boundaries given by: $\left(\frac{\rho}{R_o}\right)_n = 10^{-8}\left(1+10^{0.2(n-1)}\right)$ where n denotes the n-th ring of elements. The first ring of elements encircling the fiber-protrusion point had an outer radius $\rho/R_o = 1.0 \times 10^{-8}$. It consisted of quadratic triangular elements degenerated from the quadrilateral elements which formed the rest of the mesh. No singularity shape function or special implementation for stress singularity was incorporated into the finite elements. The θ -size of the concentric elements was 22.5^o. The mesh consisted of 389 elements. The finite element computations were performed using the ABAQUS program (Hibbitt, Karlsson and Sorensen, Inc. (1991)).

Within the spatial domain of the finite element mesh, we searched for a sub-region where the angular variation of the axisymmetric FEM-computed complete stress field , $\tilde{\sigma}^{FEM}_{ij}(\theta)$, has identical θ-dependence as that of the plane-strain singular field, $\tilde{\sigma}^1_{ij}(\theta)$, from local analysis. If the angular variation of FEM-computed stresses matches perfectly with angular variation of the singular local field (9), then the FEM-computed full-field solution has captured the eigenvector $\overline{X}$ *and* the associated eigenvalue λ_1 of the local singular field. Consequently, inside the sub-region, the FEM-computed stresses σ^{FEM}_{ij} behave with the spatial structure of the dominant local singular field (9):

$$\sigma^{FEM}_{ij} = K_1 \rho^{\lambda_1} \tilde{\sigma}^1_{ij}(\lambda_1;\theta) \tag{14}$$

Therefore, in this subregion one may choose *any* stress component, say, $\sigma_{\theta\theta}$, at *one* point at *any* angle, say θ^*, to determine K_1 :

$$K_1 = \frac{\sigma_{\theta\theta}^{FEM}(\rho^*, \theta^*)}{(\rho^*)^{\lambda} \tilde{\sigma}^1{}_{\theta\theta}(\theta^*)} \tag{15}$$

The procedure is illustrated here through an example composite material. The properties used correspond to those of Silicon Carbide (AVCO-SCS6 SiC) fiber and Borosilicate matrix. The material properties and the eigenvalue λ are given in Table 1. The local-global matching was conducted at a radius $\rho/R_0 = 5.23 \times 10^{-8}$. For an externally applied load of 1 MPa pulling at the protruded fiber end, the value of K_1 determined was 0.1145 MPa-mm$^{-\lambda}$.

In our work, we determined K_1 from $\sigma_{\theta\theta}^{FEM}$ values at the integration point closest to the fiber-matrix interface (at $\theta^* = 1.26^{o}$). If the finite element solution has indeed captured the characteristics of the local field given by (9), then the K_1 thus determined from *one* stress component at *one* θ^* value, will make *all* stress components of the finite-element results at *all* angles θ to automatically match with the singular field of (9). Figure 4 compares the angular variation of the finite-element solution with $\tilde{\sigma}_{ij}^{1}(\theta)$ of the local singularity solution. The discrete symbols represent finite element results and solid lines denote the one-term local singularity (9). That the finite element results of *all* stress components at *all* θ values indeed match the singularity solution, $\tilde{\sigma}_{ij}^{1}(\theta)$, verifies the theory and assures the accuracy of K_1 so determined. This local-global matching method by matching the entire angular variation of all stress components is tantamount to matching *both* the eigenvector and eigenvalue of the local field.

For each of the three stress components ($\sigma_{\rho\rho}$, $\sigma_{\theta\theta}$ and $\sigma_{\rho\theta}$), we define a deviation parameter $D_{ij}(\theta)$ to measure the deviation of the angular variation of FEM-stress from that of the one-term local field, $\tilde{\sigma}_{ij}^{1}(\theta)$:

$$D_{ij}(\theta) = \frac{\sigma_{ij}^{FEM}(\rho^*, \theta)}{K_1(\rho^*)^{\lambda}} - \tilde{\sigma}_{ij}^{1}(\theta) \tag{16}$$

At $\rho/R_o = 5.23 \times 10^{-8}$, the data in Figure 4 suggest $D_{ij}(\theta)$ is close to zero for all components of stresses at all θ. Similarly results were obtained for the several other composite systems studied.

Since the stress field has a singularity at O, but the finite elements surrounding O do not have special shape function to simulate unbounded stress, the matching is expected to be less than satisfactory within the very first ring of elements surrounding O. However, starting from the second ring of elements, results show good matching characteristics typical of Figure 4. It is expected that as $\frac{\rho}{Ro}$ increases beyond a certain extent, the one-term singular solution (9) deviate more from the complete full-field stresses, resulting in less spectacular angular matching at sampling points at large $\frac{\rho}{Ro}$. We can quantify this by defining a mismatch parameter, $M(\theta)$, as the root-mean-square of the deviation of the angular variation of the FEM-computed stress field from the angular variation of the one-term local field (9):

$$M(\theta) = \sqrt{\frac{1}{3}\sum_{i=1}^{3}\left(\frac{\sigma_i^{FEM}(\rho,\theta)}{K_1 \rho^{\lambda}} - \tilde{\sigma}_i^1(\theta)\right)^2} \qquad (17)$$

In (17), the following convention is used: $\sigma_1=\sigma_{\rho\rho}$, $\sigma_2=\sigma_{\theta\theta}$ and $\sigma_3=\sigma_{\rho\theta}$. $M(\theta)$ is the root mean square of the three $D_{ij}(\theta)$ components.

The value of $M(\theta)$ at different radii ρ is shown in Figure 5. Clearly, the angular mismatch depends not only upon the radial coordinate ρ but also depends upon the angular coordinate θ. The growth of the mismatch $M(\theta)$ with $\frac{\rho}{R_o}$ is due to the increasing contribution of the higher order terms, (λ_2, λ_3,...), to the complete stress field (12) at larger $\frac{\rho}{R_o}$.

To measure only the dependence on $\frac{\rho}{R_o}$, we construct an error parameter E_1 from $M(\theta)$:

$$E_1 = \frac{1}{N}\sum_{p=1}^{N}\left(\sqrt{\frac{1}{3}\sum_{i=1}^{3}\left(\frac{\sigma_i^{FEM}(\rho,\theta_p)}{K\rho^{\lambda}} - \tilde{\sigma}^1_i(\theta_p)\right)^2}\right) \tag{18}$$

E_1 is a very non-forgiving measure of mismatch error. Only *perfect* matching in *all* stress components at *all* angular positions will lead to a zero value for E_1. Figure 6 depicts the variation of E_1 as a function of $\frac{\rho}{R_o}$ in the range $10^{-8} < \frac{\rho}{R_o} < 1$ for the example composite. This plot reveals the region $10^{-8} < \frac{\rho}{R_o} < 10^{-5}$ as a reasonable domain to perform one-term matching for this particular composite system under a fiber pulling load of 1 MPa. The deviation parameter, mismatch parameter and error parameter ($D_{ij}(\theta)$, $M(\theta)$ and E_1 respectively) all measure mismatch but give different amount of detail. They are useful monitoring parameters to quantify the quality of local-global matching, and give assurance to the accuracy of K_1. They also locate the appropriate $\frac{\rho}{R_o}$ domain within which the one-term local field is dominant. With K_1 accurately determined, the dominant stress distribution (9) at the fiber protrusion point is completely solved.

The local-global matching procedure, and the associated monitoring parameters, are also applicable to problems with material nonlinearity (Lau, Argon and McClintock (1983), and Tan, Rahman and Lau (1988)). In material nonlinear problems, the linear local analysis described in Section 2 has to be replaced by asymptotic solutions for nonlinear materials.

4 Two-term Matching

The example composite system of SiC(AVCO SCS6)-Borosilicate has two singular terms, λ_1 and λ_2. In regions away from the fiber protrusion point, the dominance of the one-term field (9) reduces and higher order terms start to gain influence. The two-term local field (10) has a larger dominant region over the one-term

field (9). Although at $\rho/R_o = 5.23 \times 10^{-8}$, all components of $D_{ij}(\theta)$ are close to zero (Figure 4), at larger ρ/R_o the $D_{ij}(\theta)$ plot reveals an interesting feature. In Figure 7, the discrete symbols denote the three components of $D_{ij}(\theta)$ at $\rho/R_o = 1.57 \times 10^{-4}$. The lines denote $\tilde{\sigma}_{ij}^{2}(\theta)$, the angular variation of the second singular term (λ_2=–0.0092). This figure indicates that at $\rho/R_o = 1.57 \times 10^{-4}$ the complete stresses field (as given by the FEM-computed stresses) has captured more features of the two-term singular field, (10), than just the one-term singular field, (9). In fact, if the FEM-computed stresses exactly match the two-term singular field, according to (10) and (16) $D_{ij}(\theta)$ should match with $\tilde{\sigma}_{ij}^{2}(\theta)$ within an arbitrary scaling constant. This observation motivates a general two-term local-global matching.

Two different methods have been used to obtain both K_1 and K_2 with equal success. The first method uses directly the two-term solution in the local analysis (10). Two stress components at one spatial point or one stress component at two different spatial points are matched and a system of two linear equations is solved to obtain the amplitude factors K_1 and K_2. In this study, two different spatial points along the interface (same θ but different ρ) are chosen and the normal stresses are extracted from the global finite element analysis. Let the two points be at radii ρ_1 and ρ_2, then

$$\begin{aligned} \sigma_{\theta\theta}^{FEM}(\rho_1,0) &= K_1\rho_1^{\lambda_1} + K_2\rho_1^{\lambda_2} \\ \sigma_{\theta\theta}^{FEM}(\rho_2,0) &= K_1\rho_2^{\lambda_1} + K_2\rho_2^{\lambda_2} \end{aligned} \qquad (19)$$

These two equations are solved simultaneously to give K_1 and K_2.

The discrete symbols in Figure 8 denote the normalized FEM-computed $\sigma_{\theta\theta}$ at θ^*=2.6° (close to the fiber-matrix interface) at varies ρ/Ro. The finite element results theoretically represent the complete full-field stress distribution. The radial variation of the FEM-stresses are compared with the one-term singular field shown in dashed line, and the two-term singular field shown in solid line. The one-term field is calculated using (9) with K_1 obtained from one-term matching. The two-term field is calculated using (10) with K_1 and K_2 obtained from two-term matching. In regions close to the

fiber protrusion point, the one-term field provides a good matching with the FEM-computed stresses (see also Figure 6 at $\rho/Ro=2.53 \times 10^{-8}$). At distances away from the fiber protrusion point (say, at $\rho/Ro = 10^{-2}$), using (9) with the one-term matching does not acceptable approximation to the complete stress solution (represented by FEM results). Figure 8 shows that (10) with the two-term matching results give reasonable approxmation to the complete stress distribution up to $\rho/Ro = 10^{-1}$.

In Figure 9, finite element results are compared with the one-term singular field (9) and two-term singular field (10). The discrete symbols are the FEM-computed angular variation of stresses at $\rho^*/Ro=3.33 \times 10^{3}$. The dashed line denote the angular variation $\tilde{\sigma}_{ij}^{1}(\lambda_1;\theta)$ of the one-term field (9). The solid lines denote $S_{ij}(\theta)$ given in (20). Components of $S_{ij}(\theta)$ represent the ngular variation of stresses of the two-term field (10) at the radius $\rho = \rho^*$.

$$S_{ij}(\theta) = \left(\frac{K_1(\rho^*)^{\lambda_1} \tilde{\sigma}_{ij}^{1}(\theta) + K_2(\rho^*)^{\lambda_2} \tilde{\sigma}_{ij}^{2}(\theta)}{\sigma_{ij}^{FEM}(\rho^*,0)} \right) \tag{20}$$

The two-term matching procedure was applied to the Silicon Carbide-Borosilicate composite, for two different types applied loading: that of fiber pulling with 1 MPa, and that of thermal loading by a change of temperature of $DT= -1^{o}C$. Table 2 lists solutions of K_1 and K_2 determined by the two-term matching procedure. Also shown are results for another composite system (Nicalon fiber -Silicon Carbide matrix with E_f = 179 GPa, E_m =379 GPa, $\nu_f = 0.2$ and $\nu_m = 0.2$). The external loading for this latter case is 1MPa of applied fiber-pulling traction.

With K_1 and K_2 so determined, the locally dominant singular field is completely known (10). The relative dominance of the first and second term in the two-term field depends upon the values of λ_1 and λ_2, and the applied loading. The two parameters that govern this relative dominance are: the difference between the two eigenvalues, $(\lambda_2 - \lambda_1)$, and the ratio of the two amplitude factors $\frac{K_2}{K_1}$. The first parameter can be solved by

local analysis alone, but the latter parameter is governed by the applied loading and must be determined by two-term local-global matching.

The second method for two-term matching is based on (10) and (16). In the region in the finite element mesh where the two-term singular field (10) is dominant,

$$\sigma_{ij}^{FEM}(\rho,\theta) - K_1\rho^{\lambda_1}\tilde{\sigma}_{ij}^{1}(\theta) = K_2\rho^{\lambda_2}\tilde{\sigma}_{ij}^{2}(\theta) \tag{21}$$

and

$$D_{ij}(\theta) = \frac{\sigma_{ij}^{FEM}(\rho^*,\theta)}{K_1(\rho^*)^{\lambda}} - \tilde{\sigma}_{ij}^{1}(\theta) = \frac{K_2}{K_1}(\rho^*)^{\lambda_2-\lambda_1}\tilde{\sigma}_{ij}^{2}(\theta) \tag{22}$$

In this procedure, K_1 is first determined as described in the Section 3 from a sub-region where the one-terms singular field dominates. Then, in a further region in which the two-term singular field dominates, K_2 can be determined from angular variation matching $\tilde{\sigma}_{ij}^{2}(\theta)$ using (21) directly. Or the ratio K_2/K_1 can be determined through angular variation matching using (22). Using (21) or (22), K_2 can be obtained with the same procedure for one-term matching of Section 3.

5 Matching for Complex-valued Stress Singularity

The methodology developed in this paper is applicable to the cases of complex stress singularities with equal merit. To illustrate this fact, a hypothetical composite with the matrix modulus fifteen times greater the fiber modulus is considered. The material properties and the two complex-valued eignevalues , λ_1 and $\overline{\lambda}_1$, are listed in Table 3.

The complex-valued scaling factor, K, for problems with complex-valued singularity exponent λ_1 and $\overline{\lambda}_1$, is defined by the following equation.

$$\begin{aligned}\tau_\theta(\rho^*,0) &= \sigma_{\infty}^{FEM}(\rho^*,0) - i\sigma_{\infty}^{FEM}(\rho^*,0)\\ &= K(\rho^*)^{\lambda}\end{aligned} \tag{23}$$

or

$$K = \frac{\tau_\theta(\rho^*,0)}{(\rho^*)^{\lambda}} \tag{24}$$

The error parameter E_1 (18) can be generalized to the case of complex-valued λ as follow:

$$E_1 = \frac{1}{N}\sum_{p=1}^{N}\left(\sqrt{\frac{1}{3}\sum_{i=1}^{3}\left(\frac{\sigma_i^{FEM} - \sigma_i^{1,\,Local}}{\|K\rho^{\lambda}\|}\right)^2}\right)_p \tag{25}$$

in which

$$\|K\rho^{\lambda}\| = \sqrt{(K\rho^{\lambda})\overline{(K\rho^{\lambda})}} \tag{26}$$

The finite element mesh used for this case of complex-valued stress singularity was the same as described in Section 3. The finite-element computed interfacial normal and shear stresses are used in the local-global matching. In this example, the interfacial normal and shear stresses were determined at $\frac{\rho}{R_o} = 3.884 \times 10^{-7}$. (Note that once this radius is chosen, the complex coefficients in the local analysis have to be normalized such that the angular variation function at the interface at this radius is unity, (23). To achieve this, the complex-coefficient A_f was set to a value of (-0.013098 + i 0.018136) in the local analysis.

In the local-global matching, the complex-valued stress amplitude factor was computed from (24), giving $K = (-0.0887 - i\,0.0183563)$ corresponding to the stress singularity exponent $\lambda_1 = (-0.456 + i\,0.07291)$. The angular variation matching was found to be very satisfactory. Figure 10 shows that, with the complex-valued K so determined from one θ^* value, the singular field (denoted by lines) from local analysis agreed well with the FEM-computed stresses (discrete symbols) at *all* values of θ for *all* components of stresses. Figure 11 shows the variation of the error E_1 (24) with $\frac{\rho}{R_o}$. Comparing Figure 11 with Figure 6 (the one-term matching in a local field where there two negative λs), it seems that E_1 for the complex-valued λ is comparatively less at large $\frac{\rho}{R_o}$. The main reason for this is that the only singular terms in the complex-valued case

are due to λ_1 and $\overline{\lambda}_1$. Since λ_1 and $\overline{\lambda}_1$ are complex conjugates with identical real parts, this complex-valued matching has incorporated all the singular terms in the local-global matching. On the contrary, the one-term matching results of Figure 6 has not considered the other admissible singular term , λ_2. Therefore, at large $\frac{\rho}{R_o}$ the neglected λ_2 term contributes to E_1 in Figure 6.

6 Comparison with Purely Finite Element Estimation

Without conducting local analysis to determine λ and $\tilde{\sigma}_{ij}(\theta)$, but assuming the local stresses is a one-term singular field of the form: $\sigma_{ij}(\rho,\theta) = K\rho^{\lambda}\tilde{\sigma}_{ij}(\theta)$ where λ is real-valued, one may use finite element results alone to estimate λ and K. The finite element estimation techniques generally involve finding the slope of the radial variation of the stress components on a log-log scale. Figures 12(a) and 12 (b) show such log-log plots to estimate λ using the finite element results from our global analysis. From Figures 12(a) and (b), it is clear that the value of λ so estimated from purely finite element results varies in magnitude depending on which stress component is used and which angle θ is used.

The stress amplitude factor K can also be estimated using purely finite element results. In such estimation of K one needs first the value of λ. Since the λ estimated from finite element results has a range of values depending on the stress component used or the θ used, this uncertainty is passed on to the value of K when K is estimated. There is no good means to quantify the error in estimating K and λ using purely finite element results. Without solving the local singularity a priori, there is little assurance on the accuracy of K estimated from the finite element results.

On the other hand, a prior knowledge of the singularity exponent λ helps guide to determine K accurately. For crack problems, knowing that $\lambda = -0.5$ helps guide the use of finite element results to solve for stress intensity factor. For the free edge

interface in bimaterials, Munz and Yang (1992) first solved λ by Bogy's (1971) approach to guide subsequent use of finite element results to determine K accurately. For problems where λ is not known, it is recommended to conduct first a local analysis before using finite element results. In the local analysis, other than calculating just λ it is worth a researcher's time to determine also the angular variation of stresses. With both the λ and angular variation known, in subsequent local-global matching the researcher can seek to match *both* the eigenvalue and eigenvector to ensure more reliable results.

Application of purely finite element results in log-log plots to estimate λ and K does not work well to solve for the two-term singular field (10) should it exists. Although the example composite system Silcon Carbide-Borosilicate has two singular terms λ_1 and λ_2 (Table 2), the finite element results does not show any change in slope (Figures 12(a) and (b)). Consequently, without local analysis, just the finite element results would not have enough resolution to solve for both λ_1 and λ_2, and both K_1 and K_2.

When the stress field has complex-valued λ, then finite element estimation techniques based on radial variation of stresses (Figures 12(a) and 12(b)) would not work. With complex-valued λ, a typical stress component, say $\sigma_{\theta\theta}$, is of the form

$$\sigma_{\theta\theta} = \mathrm{Re}(\tau_\theta) = \mathrm{Re}\left[K\rho^\lambda F_\theta(\cos(\varepsilon\log\rho),\sin(\varepsilon\log\rho),\lambda,\theta)\right], \quad (\text{where, } \varepsilon = \mathrm{Im}[\lambda])$$

which shows stress oscillation with respect to ρ. On the other hand, the local-global matching method presented in previous sections, is applicable to stress fields with complex-valued λ.

A relative advantage of the local-global matching method is that the monitoring parameters $D_{ij}(\theta)$, $M(\theta)$ and E_1 can be used to measure the quality of matching. Use of these quality control parameters can ensures an accurate determination of K by verifying that the finite-element computed stresses used in matching indeed has captured the full spatial characteristics of the asymptotic singular solution in the space (domain) of matching.

7 Concluding Remarks

The local analysis presented can determine the detail spatial structure of singular stress field at the fiber protrusion point. For the problems considered here, both one-term singular field and two-term singular field are possible. In some composite materials, the singularity exponent can be complex-valued.

The local-global matching method can determine the amplitude factors accurately for the one-term field and two-term field with real-valued singularity exponent. It is based on angular variation matching which is tantamount to matching both the eigenvalue and eigenvector of the asymptotic field. It is recommended that in local analysis, not just the singularity exponent λ but also the angular variation of stresses should be determined so one can match the eigen-pair instead of just matching the eigenvalue in subsequent local-global matching.

The monitoring parameters $D_{ij}(\theta)$, $M(\theta)$ and E_1 can provide quantifiable measures of the quality of local-global matching.

In its generalized form, the local-global matching is equally applicable to cases with complex-valued singularity exponent to determine complex-valued amplitude factor.

The local-global matching method can be applied for other interfacial conditions such as frictional sliding and interfacial crack.

With minor modification, the local-global matching method is also applicable to material nonlinearity problems.

ACKNOWLEDGMENTS

This work was partially supported by a grant from the Air Force Office of Scientific research and by Drexel University. This support is gratefully acknowledged.

REFERENCES

Atkinson, C., Avila, J., Betz, E. and Smelser, R. E., (1982), The rod pullout problem, Theory and Experiment, *J. Mech. Phys. of Solids*, 30, 97-120.

Bogy, D. B., (1971) Two edge bonded elastic wedges of different materials and wedge angles under surface tractions, J. Appl. Mech., 93, 377-386.

Carpenter, W. C., (1985), Calculation of fracture mechanics parameters for a general corner, Int. J. Fracture, 24 45-58.

Dempsey, J. P. and Sinclair, G. B., (1981), On the singular behavior at the vertex of a bi-material wedge, J. Elast., 11, 317-327.

Dundurs, J., (1969), Discussion on Edge bonded dissimilar othogonal elastic wedges under normal and shear loading, J. appl. Mech., **36** , pp. 650-651.

England, A.H, (1971), *Complex variable methods in elasticity*, Wiley Interscience, London.

Evans, A. G. and Marshall D. B., (1989), The mechanical behavior of ceramic matrix composites, Acta Metall, 37, 2567-2583.

Greszczuk, L. B., (1969) Theoretical studies of the mechanics of the fiber-matrix interface in composites, Interefaces in composites, ASTM STP-452, American Society for Testing and Materials, Philadelphia, PA.

Hein, V. L. and Erdogan, F. (1971), Stress singularities in a two material wedge, Int. J. Fracture, 7 , 317.

Hibbitt, Karlsson and Sorensen, Inc. (1991), ABAQUS user's manual, Pawtucket, RI 02860 USA.

Hutchinson, J. W. and Jensen, H. M., (1990), Models of fiber debonding and pull-out in Brittle composites with friction, Mech. Mater., 9, 139-163.

Iancu, O. T., Fett, T., and Munz, D. (1990), A fracture mechanical treatment of free edge stress singularities applied to a brazed ceramic/metal compound, Int. J. Fracture, 46, 159-172.

Kerans, R. J., Hay, R. S., Pagano, N. J. and Parthasarathy, T. A., (1989), The role of the fiber-matrix interface in ceramic composites, Ceram. Bull., 68, 429-442.

Kurtz, R. D. and Pagano, N. J., (1991), Analysis of the deformation of a symmetrically loaded fiber embedded in a matrix material, Composites Engineering, 1, 13-27.

Lau, C. W. , Argon, A. S., and McClintock, F. A., (1983), Application of the finite method in micromechanical analyses of creep fracture problems, Computers and Structures, 17, 923-931.

McCartney, L. N., (1989), New theoretical model of stress transfer between fiber and matrix ina a uniaxially fiber-reinforced composite, Proc. R. Soc. of London, A 425, 215-244.

Moré, Jorge, Garbow B. and Hillstrom, K, (1980), *Users Guide For MINPACK-1*, Argonne National Laboratories Report ANL-80-74, Argonne, Illinois .

Munz, D and Yang, Y. Y., (1992), Stress singularities at the interface in bonded dissimilar materials under mechanical and thermal loading, J. Appl. Mech., 59, 857-861.

Pochiraju, K. V., Lau, A. C. W. and Wang, A. S. D, (1992) On fiber-matrix interfacial stresses during fiber pullout with thermal stressing, Proceedings of the Seventh Technical Conference, American Society for Composites, Technomic Publishing Co., Lancaster, PA., 827-837.

Pochiraju, K. V., (1993), Mechanics of the single fiber pullout problem with several interface conditions, Ph. D. Dissertation, Drexel University, Mechanical Engineering and Mechanics, Philadelphia, PA 19104, USA.

Pochiraju, K. V., Lau, A. C. W., and Wang, A. S. D. (1993), Characteristics of Stress distributions in the single fiber pullout problem with perfectly bonded interface, in preparation.

Tan, T. M., Lau, A. C. W. and Rahman, A , (1989), Interfacial micro-mechanics of hybrid metal matrix composites, Proceedings of American Society of Composites symposium on high temperature composites, Technomic Publishing Co., Lancaster, PA., 72-85.

Zak, A. R., (1964), Stress in the vicinity of boundary discontinuities in bodies of revolution, J. appl. Mech. 33 , 150-152.

Table 1: Material properties and singularity exponents, λ_1 and λ_2, for the Silicon Carbide-Borosilicate system.

E_m	E_f	ν_m	ν_f	$\alpha_m-\alpha_f$ x 10^{-5}	Fiber Radius (R_o)	λ_1	λ_2
63 GPa	410 GPa	0.2	0.2	7.2 / ^oC	71.5 μm	–0.313344	–0.0092246

Table 2: Amplitude factors for the first and second singular terms for three example problems.

Material/ (Loading Type)	λ_1	λ_2	K_1 MPa/(mm)$^{\lambda 1}$	K_2 MPa/(mm)$^{\lambda 2}$
Sic-Borosilicate (Pulling-1 MPa)	–0.313344	–0.00922466	0.1153	–0.2998916
Sic-Borosilicate (DT= –1^oC)	–0.313344	–0.00922466	0.0333911	–0.12094
Ni- Sic (Pulling-1 MPa)	–0.4914585	–0.1747356	0.01458	–0.05103

Table 3: Material properties of the hypothetical composite system having complex-valued singularity exponents, λ_1 and $\overline{\lambda}_1$

E_m	E_f	ν_m	ν_f	$(\alpha_m-\alpha_f)$ x 10^{-5}	Fiber Radius R_o	λ_1	$\overline{\lambda}_1$
15 GPa	1 GPa	0.2	0.2	1 / ^oC	71.5 μm	(–0.456 + i 0.07291)	(– 0.456 – i 0.07291)

Legends to Figures

Figure: 1. Schematics of the single fiber pullout model showing local and global co-ordinate systems.

Figure 2: Variation of the exponent of stress singularity λ with material properties

Figure: 3. Schematics of the finite element mesh

Figure 4: Comparison of angular variation of FEM-computed stresses (discrete symbols) with one-term singular field (lines) at $\rho/R_o = 5.3\times10^{-8}$ for an example composite Silcon Carbide-Borosilicate (SiC-Borosilicate).

Figure 5: Variation of the mismatch parameter $M(\theta)$ with θ in one-term matching

Figure 6: Variation of the error parameter E_1 with ρ/R_o in one-term matching.

Figure 7: Comparison between $D_{ij}(\theta)$ and $\tilde{\sigma}_{ij}^{2}(\theta)$ at $\rho/R_o = 1.57\times10^{-4}$.

Figure 8: Comparison of FEM-computed full-field stress (discrete symbols) with one-term singular field (dashed line) and two-term singular field (solid line) for the SiC-Borosilicate example composite.

Figure 9: Comparison of FEM-computed angular variation with $\tilde{\sigma}_{ij}^{1}(\lambda_1;\theta)$ and $S_{ij}(\theta)$ at $r/R_o = 3.33\times10^{-3}$ for the SiC-Borosilicate example composite.

Figure 10: Angular variation matching for composite with complex-valued stress singularity exponent, $r/R_o = 5.28\times10^{-8}$.

Figure 11: Variation of the error parameter E_1 with ρ/R_o for composite with complex-valued stress singularity exponent.

Figure 12 (a): Estimation of the exponent of singularity λ based radial variation of finite element results of two stress components.

Figure 12 (b): Estimation of the exponent of singularity λ based radial variation of finite element results of $\sigma_{\theta\theta}$ at three different angles.

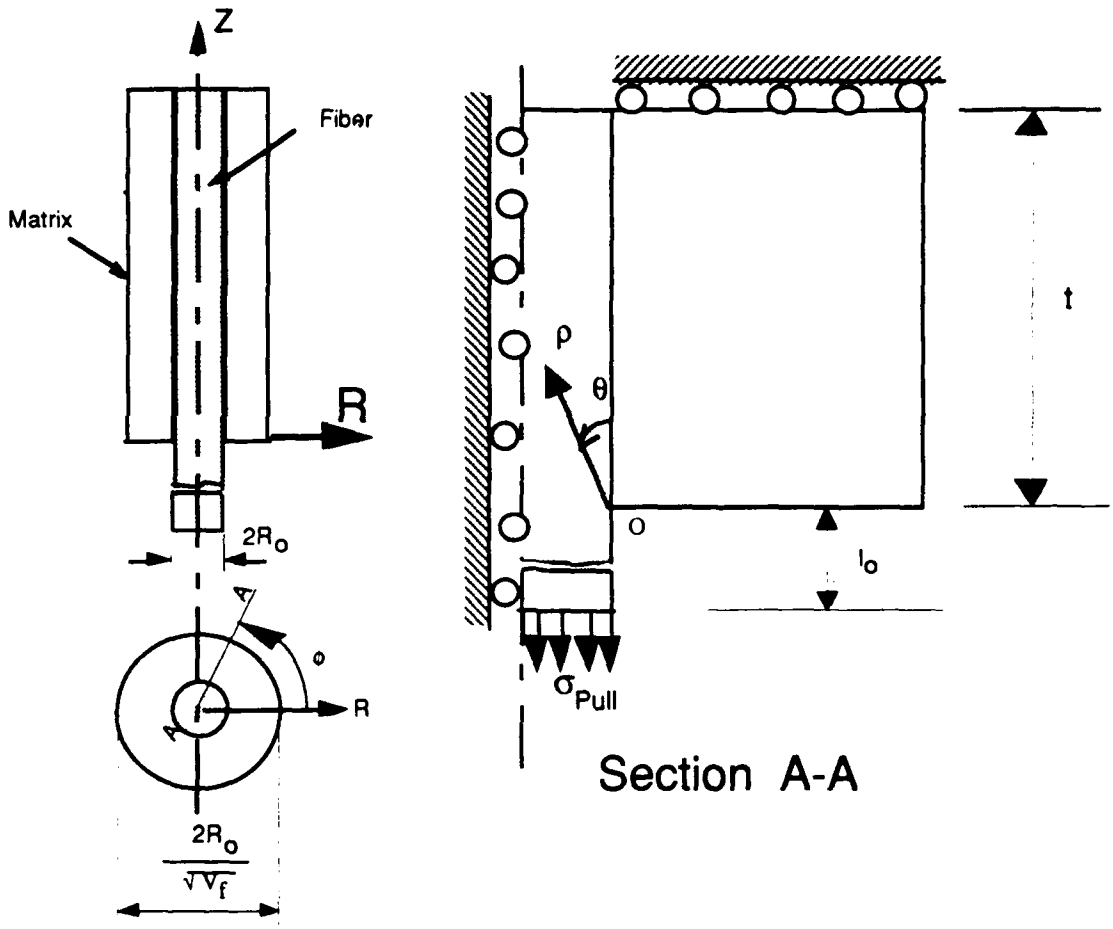

Figure: 1. Schematics of the single fiber pullout model showing local and global co-ordinate systems.

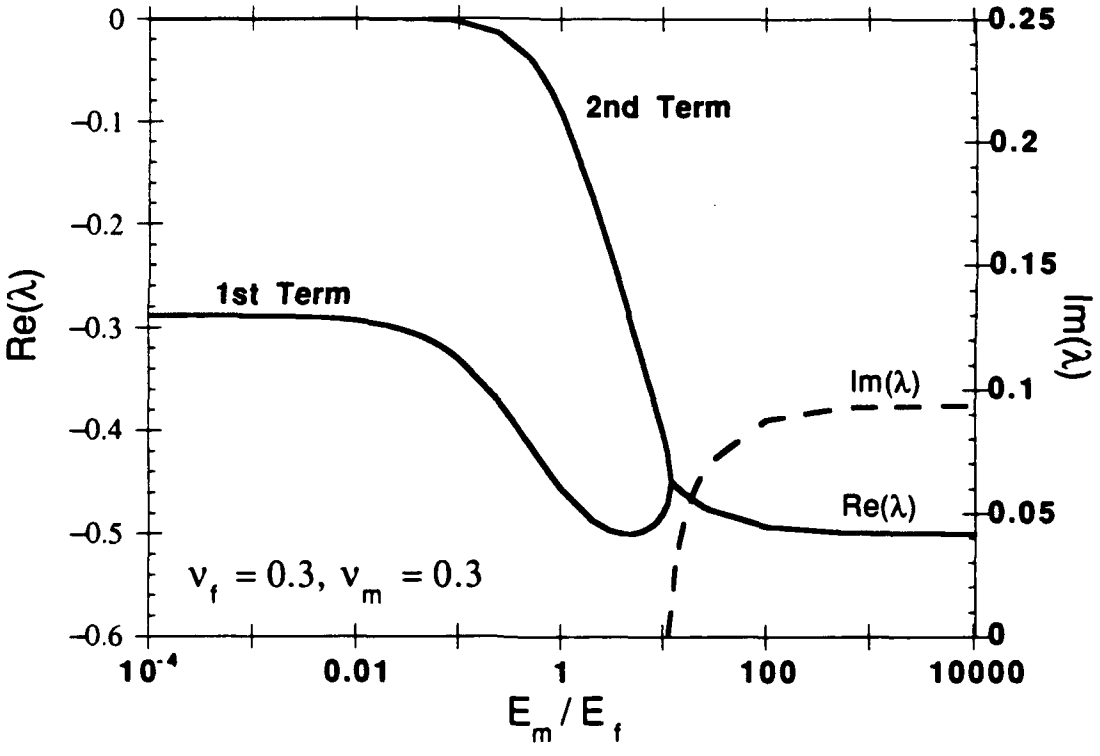

Figure 2: Variation of the exponent of stress singularity λ with material properties

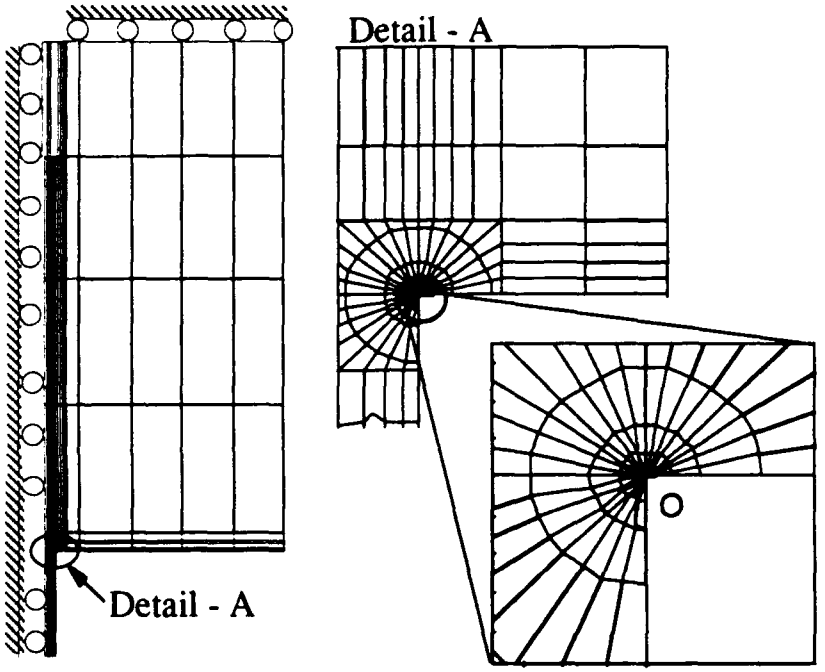

Figure: 3. Schematics of the finite element mesh

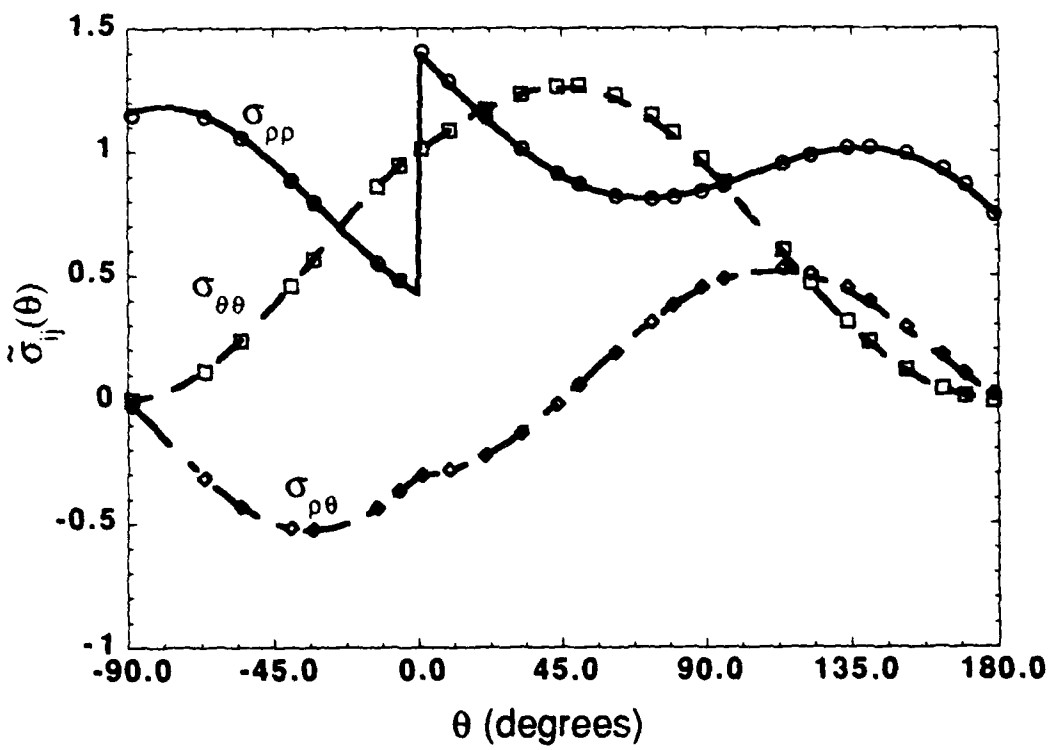

Figure 4: Comparison of angular variation of FEM-computed stresses (discrete symbols) with one-term singular field (lines) at $\rho/Ro = 5.3 \times 10^{-8}$ for an example composite Silcon Carbide-Borosilicate (SiC-Borosilicate).

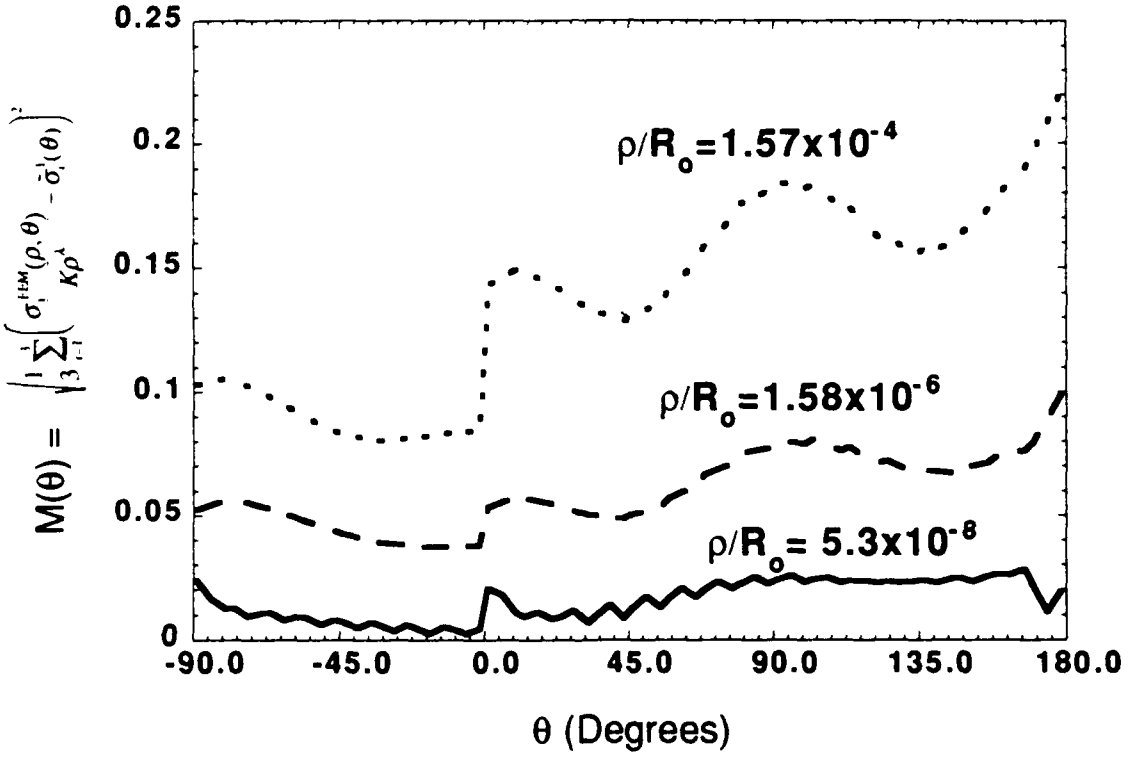

Figure 5: Variation of the mismatch parameter $M(\theta)$ with θ in one-term matching

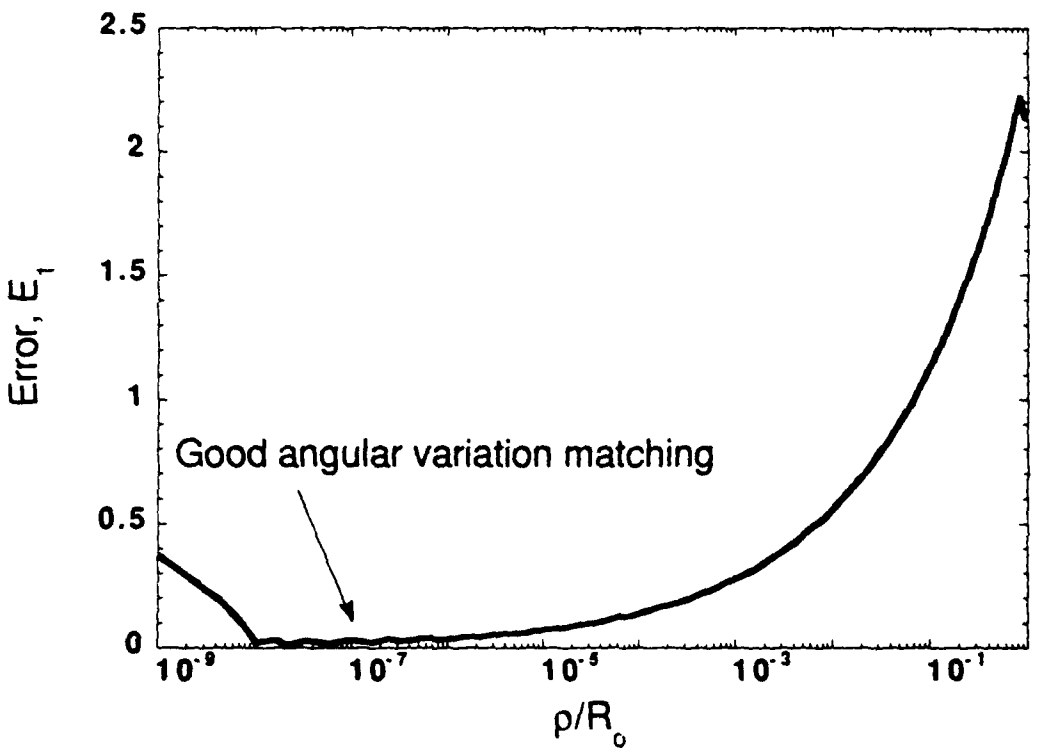

Figure 6: Variation of the error parameter E_1 with ρ/R_O in one-term matching.

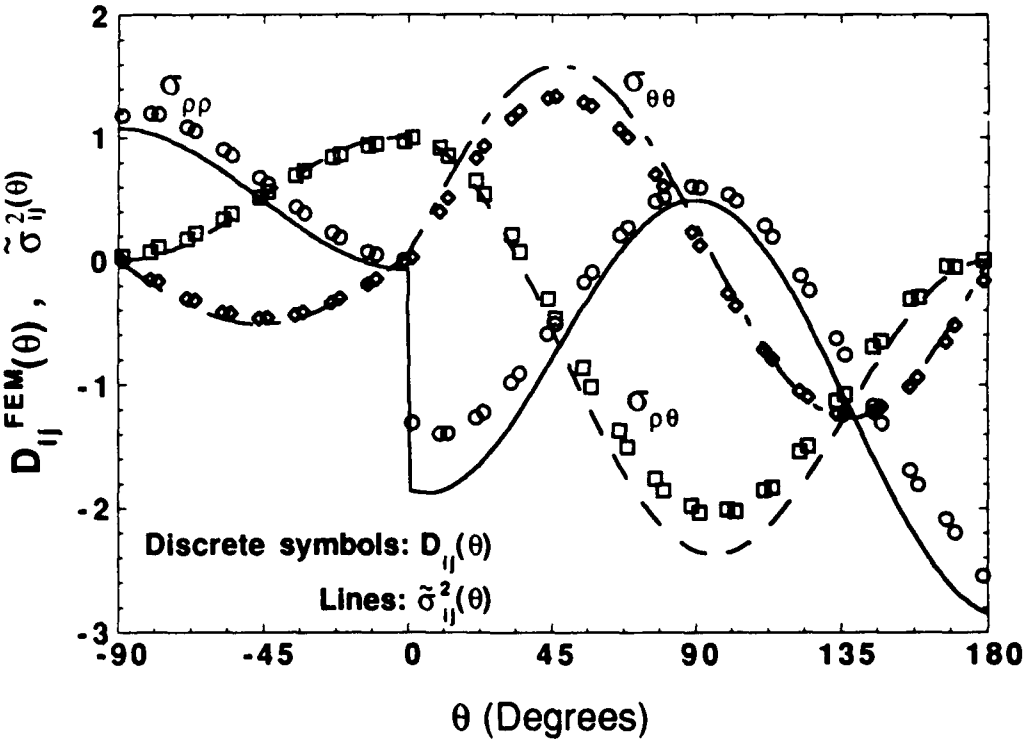

Figure 7: Comparison between $D_{ij}(\theta)$ and $\tilde{\sigma}_{ij}^{2}(\theta)$ at $\rho/R_o=1.57\times10^{-4}$.

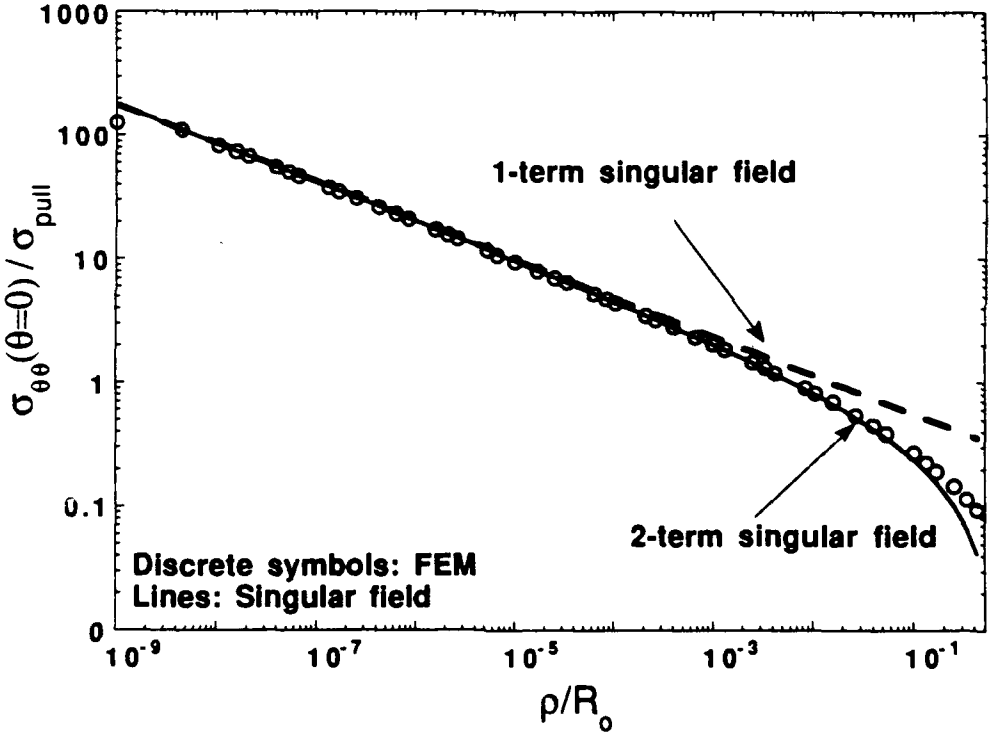

Figure 8: Comparison of FEM-computed full-field stress (discrete symbols) with one-term singular field (dashed line) and two-term singular field (solid line) for the SiC-Borosilicate example composite.

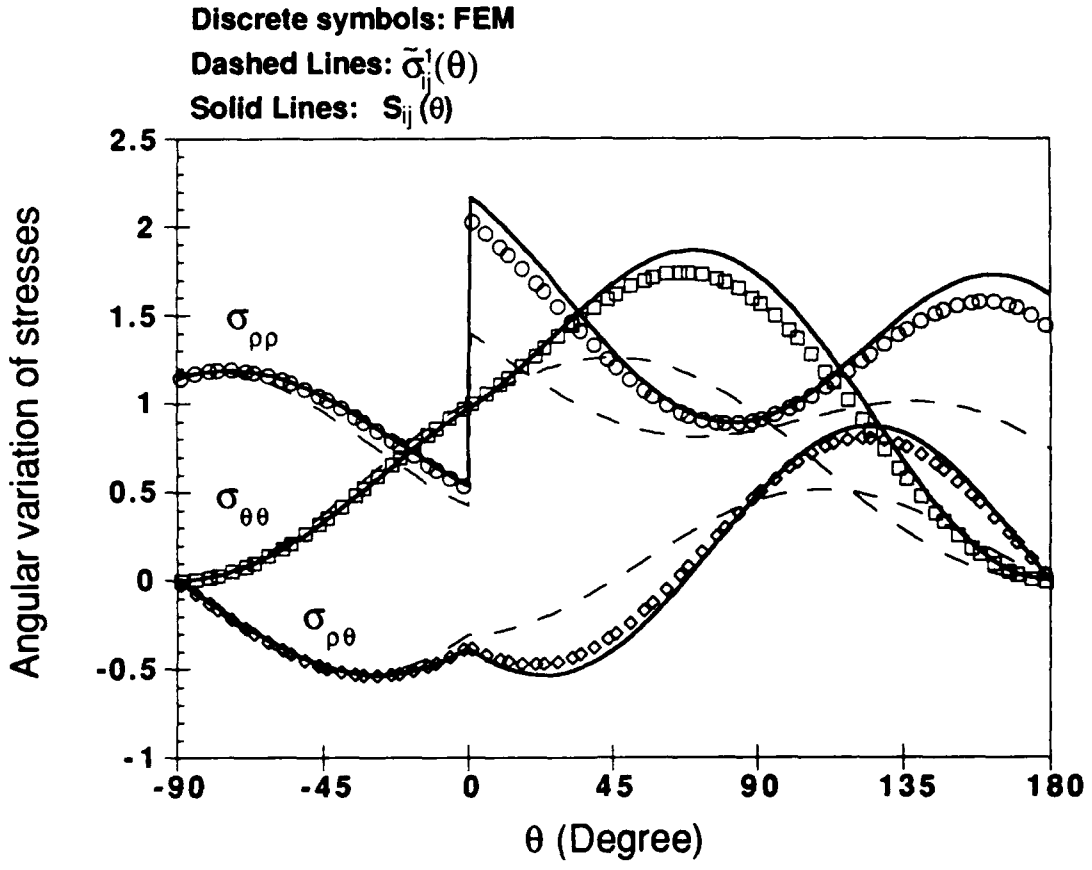

Figure 9: Comparison of FEM-computed angular variation with $\tilde{\sigma}^1_{ij}(\lambda_1;\theta)$ and $S_{ij}(\theta)$ at $r/R_O=3.33x10^{-3}$ for the SiC-Borosilicate example composite.

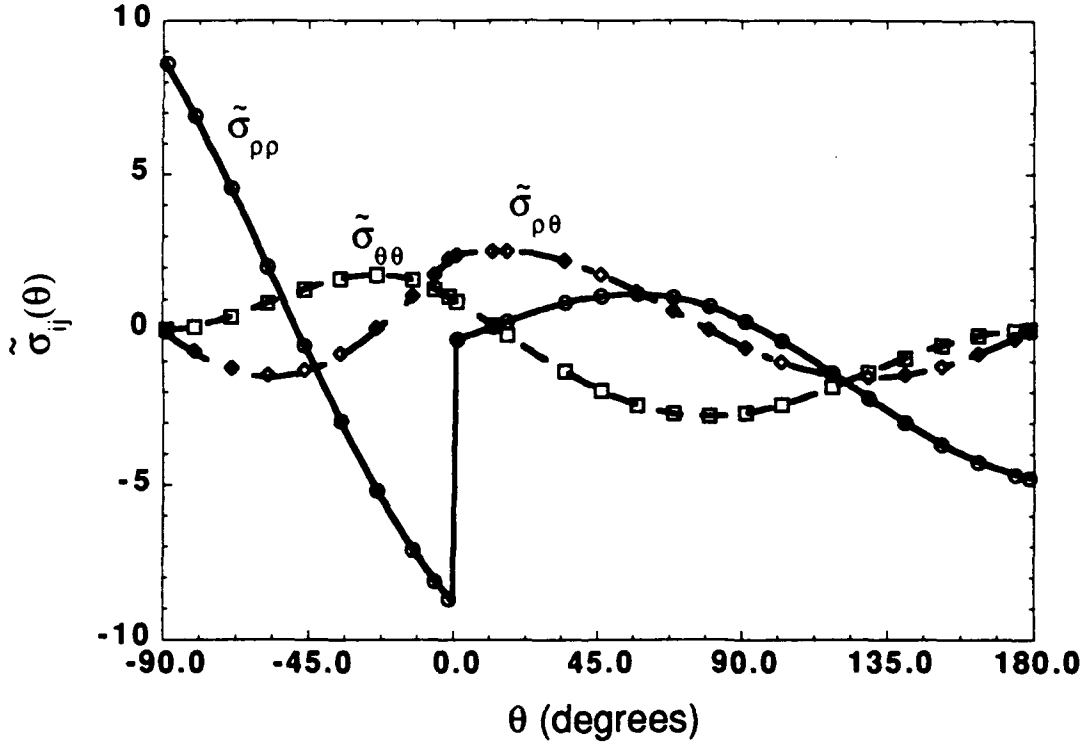

Figure 10: Angular variation matching for composite with complex-valued stress singularity exponent, $r/R_o = 5.28 \times 10^{-8}$.

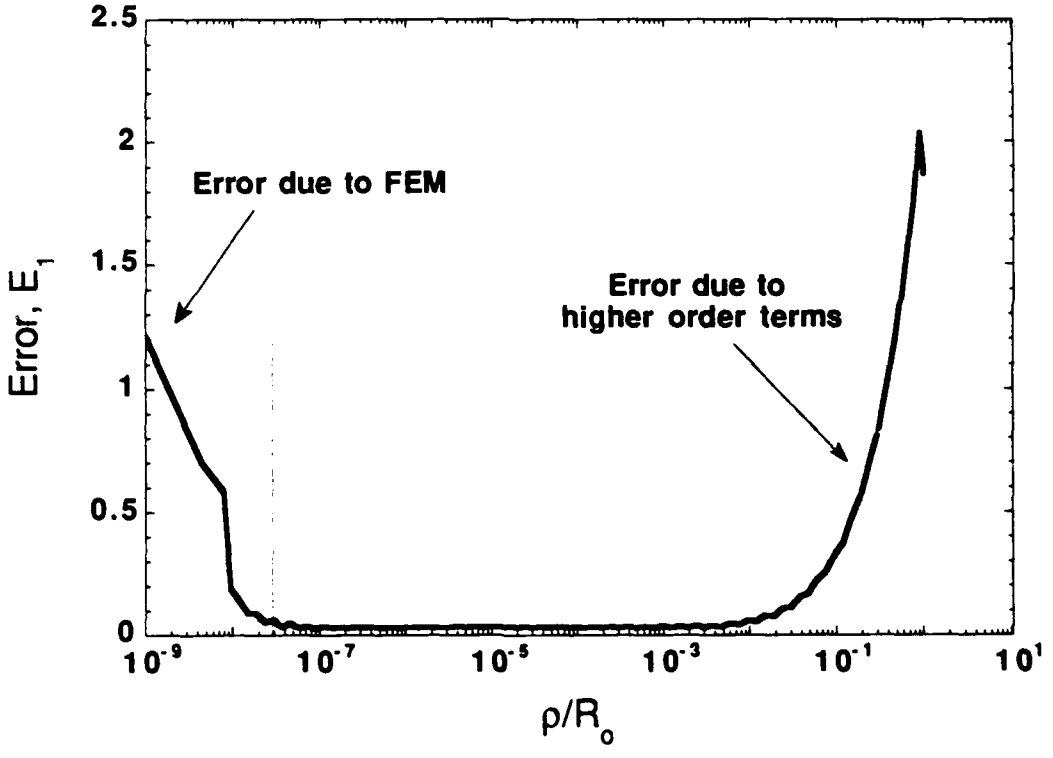

Figure 11: Variation of the error parameter E_1 with ρ/R_o for composite with complex-valued stress singularity exponent.

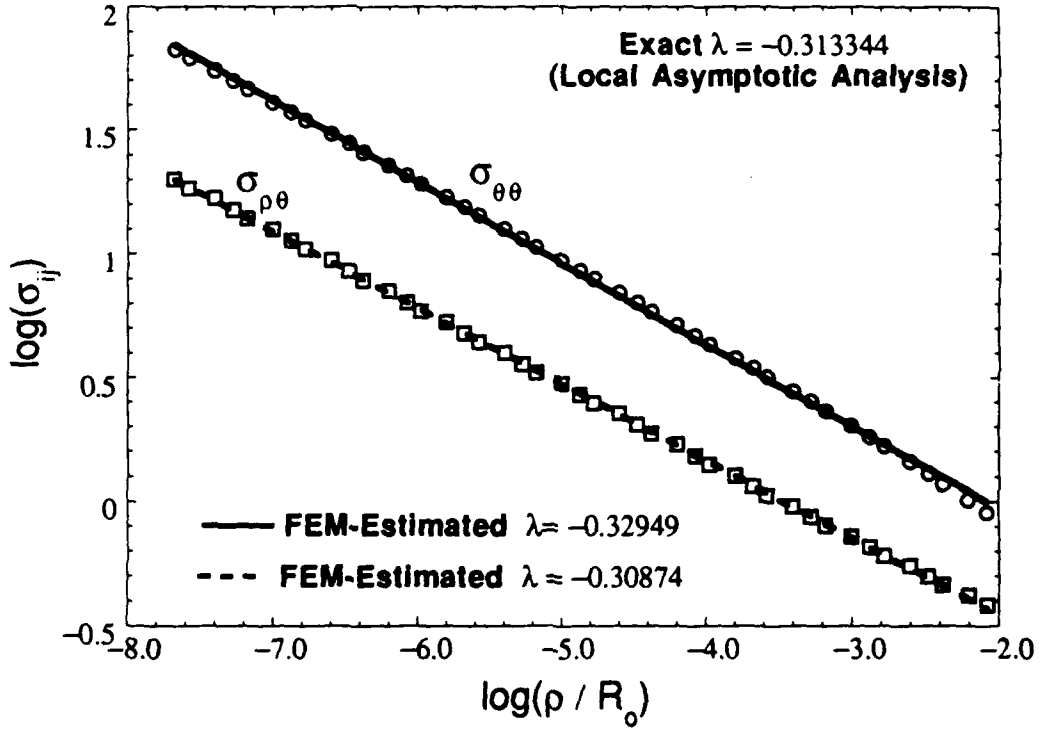

Figure 12 (a): Estimation of the exponent of singularity λ based on radial variation of finite element results of two stress components.

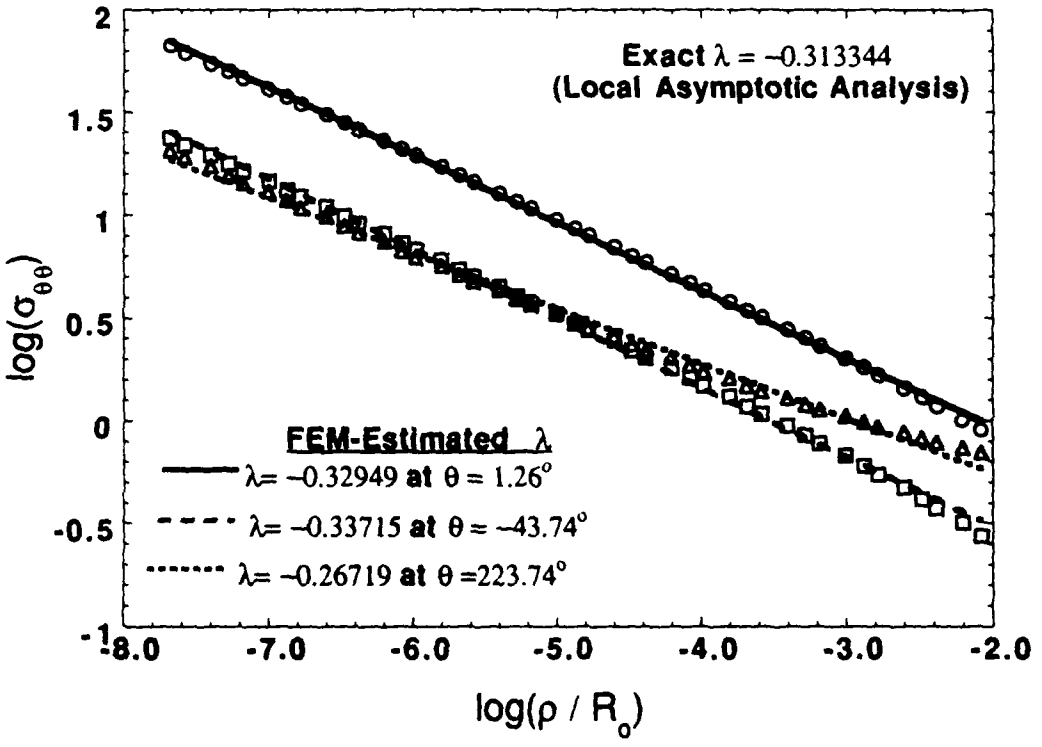

Figure 12 (b): Estimation of the exponent of singularity λ based on radial variation of finite element results of $\sigma_{\theta\theta}$ at three different angles.

journal

Thermal Expansion of Siiicon Carbide Monofilaments and Silicon Carbide–Borosilicate Composites

Alexander Elkind, Michel Barsoum*, and Pramod Kangutkar*

Materials Engineering Department, Drexel University, Philadelphia, Pennsylvania 19104

The coefficient of thermal expansion (CTE) of a 140-μm-diameter SiC monofilament was determined to be 6.5 ± 0.5 × 10^{-6}°C^{-1} in the temperature range 25°–900°C. Heat treatment of the fibers at 1400°C for 90 min resulted in both an increase in the intensities of the SiC peaks and a reduction of their width, indicating some grain growth. Furthermore, heat treatment of the fibers for 2 h at 1600°C in vacuum reduced their CTE to 5.7 × 10^{-6}°C^{-1}. The anomalously high CTE and its decrease upon heat treatment were attributed to the presence of a large fraction of the atoms in the boundaries between the nanometer β-SiC grains. The thermal expansion coefficients of a series of SiC/borosilicate composites were measured as a function of fiber volume fraction in the temperature range 25°–500°C and found to follow the rule of mixtures.

I. Introduction

In designing ceramic/ceramic composites one of the more important considerations is the thermal compatibility between the reinforcing phase and that of the matrix. For fiber-reinforced ceramic matrix composites both the radial and the axial thermal expansion mismatches are important. If the fibers have a larger coefficient of thermal expansion (CTE) than the matrix, then, upon cooling from the processing temperature, the matrix will be in axial compression. Radially the fiber/matrix interface will be in tension and will tend to debond. Conversely, if the CTE of the fibers is lower than the matrix, the latter will radially clamp down on the fibers upon cooling, but the matrix will experience an axial residual tensile stress. In either case, degradation in the mechanical properties of the composites can result.

One of the more promising fibers for reinforcing ceramic matrices is the SCS-6 SiC monofilament (Textron Specialty Materials, Lowell, MA). In addition to its high intrinsic strength and stiffness, it is fairly oxidation resistant. This fiber is manufactured by chemical vapor deposition of SiC onto a 35-μm carbon core. A micrograph of the cross-section of the fiber is shown in Fig. 1. The SiC grains, composed mainly of β-SiC, are heavily faulted, radially oriented, and columnar with the octahedral planes preferentially oriented to the deposition surface.[1] The graphitic carbon coating on the fiber surface is not pure, but has been shown to have SiC particles embedded in it.[2]

The radial and axial thermal expansion coefficients of SCS-6 monofilaments have been measured by various investigators[3–9] and the results are summarized in Table I. The values for the axial CTE's range from 4 × 10^{-6}°C^{-1} to 5.5 × 10^{-6}°C^{-1}. Although part of the scatter can be attributed to the different temperature ranges investigated, the range is quite wide. As will be discussed in more detail below, another possible source of variability may be differences in the amorphous phase content between different manufactured fiber lots.

Fig. 1. Micrograph of SiC monofilament.

The reported values for the radial CTE's also vary (see Table I). As far as can be traced, the only direct measurement was conducted by Goettler and Faber.[6] Other values reported[5,7,8] were inferred from stress birefringence measurements conducted at room temperature as the thermal expansion of the matrices were varied. In one study,[5] the decrease in interfacial shear stress required to pull out single fibers from a borosilicate matrix as the temperature increased was taken as evidence that the radial CTE of the fibers was less than the matrix, i.e., <3.2 × 10^{-6}°C^{-1}.

Table I. Summary of Reported Values of CTE of SCS-6 Fibers and Composites

Temp Range (°C)	CTE × 10^{6}°C^{-1}	Comments	Ref
Axial			
400-1350	5.2	Taken from Fig. 4 in Ref. 3	3
600-1200	5.0	Taken from Fig. 5 in Ref. 3 Pronounced shrinkage observed at 1360°C	3
800-1300	5.5	Taken from Fig. 7 in Ref. 4	4
25-500	3.99	Dilatometry (data was not shown).	5
25-900	6.5 ± 0.5	This work.	
Radial			
	2.63	Dilatometry	6
	< 4.0	Based on stress birefringence measurements	5
	< 3.2	Based on stress birefringence measurements	7
	< 3.2	Based on stress birefringence measurements	8
	< 3.2	Measurement of relaxation of residual stresses	9

D. K. Shetty—contributing editor

Manuscript No. 195736. Received April 27, 1992, approved July 7, 1992.
Partially supported by the Air Force Office of Scientific Research under Contract No. 90-0172.
*Member, American Ceramic Society

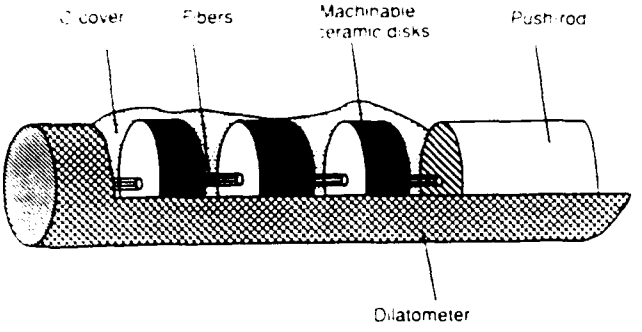

Fig. 2. Schematic of sample holder used for measuring the axial thermal expansion of the fibers.

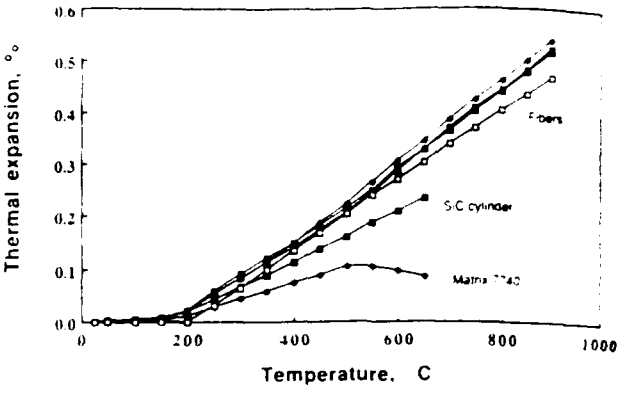

Fig. 3. Functional dependence of axial thermal expansion of the SiC monofilaments on temperature in the 25°–900°C range. The top four curves are for four different fiber batches. The middle curve (open squares) is for monolithic dense SiC. The bottom curve is for 7740 borosilicate glass.

The objective of this work was to measure the axial thermal expansion of SCS-6 SiC monofilament and composites made using these fibers in an attempt to better quantify and understand their thermal expansion behavior.

II. Experimental Procedure

(1) *Fiber Thermal Expansion*

The axial thermal expansion of the SiC monofilaments (grade SCS-6, AVCO Specialty Materials, Textron, Inc., Lowell, MA) was measured using the sample holder shown schematically in Fig. 2. To align the fibers and keep them from buckling, 8–10 fibers (10–12 mm long) were inserted through holes drilled in the centers of ceramic disks machined out of machinable ceramics, such that ≈2 mm of fibers protruded on either side. The disks in turn were placed in a dilatometer (Model No. TDA-H1 with an alumina holder, Harrop Industries, Columbus, OH) and the thermal expansion was measured in the temperature range between room temperature and 900°C. The fibers were free to slide through the ceramic disks at all times and no reaction was observed between the fibers and the disks.

The sample temperature was measured using a thermocouple placed as close as possible to the fibers. Heating the fibers at temperatures >1000°C resulted in significant shrinkage. This shrinkage is believed to be due to buckling and/or creep of the fibers under the push-rod loading.

Preliminary runs indicated that good thermal contact between the fibers and the dilatometer fixture, together with slow heating rates, gave the most reproducible results. The heating rate was 5°C/min. To ensure good thermal contact, as well as completely shield the fibers from oxidation, the whole assembly was covered with a graphite powder as shown in Fig. 2. Ar gas was passed over the samples at all times. All the data presented here were obtained with the C-cover and under a flowing atmosphere of Ar. Nevertheless, the thermal expansion at temperatures below 200°C were anomalously low; the reason for this is not entirely clear but could possibly be due to a thermal lag between the thermocouple and the fibers. This behavior is not uncommon for this type of dilatometer.

The dilatometer was calibrated by measuring the thermal expansion of fused quartz, a borosilicate glass (7740, Corning Glass Works, Corning, NY), and a monolithic, fully dense SiC cylinder. In all cases the measured values agreed with the published results.

(2) *Thermal Expansion of Composites*

Unidirectional reinforced composites were fabricated by vacuum hot-pressing borosilicate glass powders and the SiC monofilaments at 1200°C for 10 min. The details of the fabrication procedure can be found elsewhere.[10] The fiber volume fraction of each specimen was individually measured by determining the total fiber area in the specimen's cross section. Bars, 10–20 mm long, of square cross section (2 mm × 2 mm) were used for the measurements. The temperature range over which the thermal expansion could be measured was limited on the high side by the dilatometric softening point, (≈550°C) of the borosilicate glass matrix. The CTE of the hot-pressed glass matrix was also measured (see Fig. 3) and found to be 3.1×10^{-6}°C, in agreement with manufacturer's data sheet.

III. Results and Discussion

(1) *Thermal Expansion of Fibers*

The temperature dependence of the fiber displacements in the temperature range 25°–900°C for four different fiber samples is shown in Fig. 3. The corresponding CTE in the temperature range 200°–900°C is $6.5 \pm 0.5 \times 10^{-6}$°C^{-1}. This value is higher than any of the reported values to date (see Table I). Also included in Fig. 3 are the results of a monolithic block of dense SiC, where the measured CTE is calculated to be 4.5×10^{-6}°C^{-1}. It is worth noting that this value is significantly lower than that of the fibers.

Treating the fiber as a composite with a C-core in a SiC matrix ($V_{core} = 8\%$, $E_{core} = 40$ GPa, and $\alpha_{core} = 10 \times 10^{-6}$°C^{-1} (Ref. 11) and $E_{SiC} = 440$ GPa) and using Eq. 1 (see below), the calculated fiber CTE is 4.54×10^{-6}°C^{-1} which clearly cannot account for the CTE value measured here. The thermal expansion anisotropy[12] of SiC is also not sufficient to explain the anomalously high α of the fibers.

X-ray diffraction (XRD) of the as-received fibers shows them to be composed of β-SiC. However, TEM observations carried out by Wawner *et al.*[13,14] have shown that the bulk of these SiC monofilaments consisted of columnar β-SiC subgrains which were 30–100 nm in size. This implies that a large fraction of the atoms are residing in the grain boundary areas. We propose that these atoms, which can be considered to be an amorphous or grain boundary "phase," are responsible for the higher CTE of the fibers as compared to monolithic SiC. To test this hypothesis a number of fibers were covered in graphite and heat-treated at 1400°C under flowing Ar for 90 min. The X-ray powder diffraction of the as-received and heat treated samples, with an MgO internal standard, is shown in Fig. 4. These measurements were repeated on three different batches of fibers with similar results. Both an *increase* in the intensity of the SiC peaks and a *decrease* in the full width at one-half maximum of the peaks were observed as a result of the heat treatment. These results are clear and unambiguous evidence for the increase in crystallinity of the samples and the occurrence of grain growth. From the X-ray line broadening, using the Scherrer formula, the average crystallite size was calculated to be 25 nm for

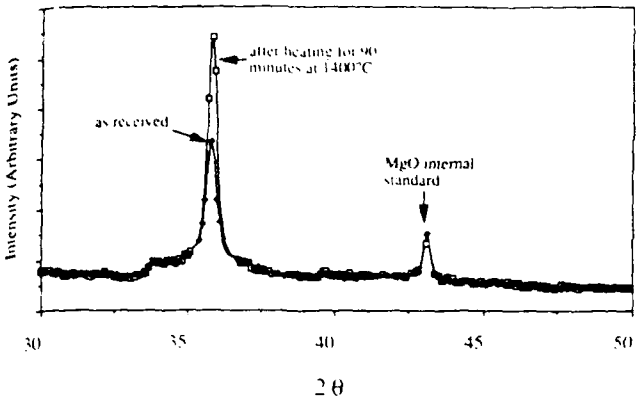

Fig. 4. X-ray powder diffraction of as-received fibers (solid diamonds) and fibers that were heat treated at 1400°C for 90 min (open squares). The peak on the right is that of the MgO standard.

as-received fibers and 50 nm for the heat treated ones, which is in good agreement with the values reported by Wawner *et al.*

An implication of this hypothesis is, that the amorphous content of the fibers influences their CTE's. To test this hypothesis, the CTE of a set of fibers that were heat-treated in vacuum (≈0.1 Pa) for 2 h at 1500°C was measured. The CTE dropped to 5.7×10^{-6} °C^{-1}, which is lower than the value for the as-received fibers. From the work conducted here, what remains unclear is the distribution, volume fraction, and thermal expansion of the amorphous phase. Further work would have to be conducted to explore this issue.

There is indirect evidence in the literature for the occurrence of structural changes in these fibers in the temperature range 900°–1400°C. Based on creep measurements DiCarlo[4] concluded that thermally induced microstructural changes that reduce the creep rate occurred between 1200° and 1400°C. Furthermore, McHenery and Tressler[11] observed a strength degradation in the 900°–1000°C range and speculated that recrystallization and/or grain growth of the SiC may be responsible. However, their XRD and SEM analysis failed to identify a specific mechanism. Crystallization of an amorphous grain-boundary phase and/or grain growth could explain both observations.

It is thus possible, that during manufacturing variations in processing variables could have resulted in variations in the grain size or amorphous content of the fibers. This would not only explain the variability in the CTE values measured between various investigators, but also explain the anomalously high values of CTE measured here. It would also explain the variability in shrinkage reported from lot to lot.[3]

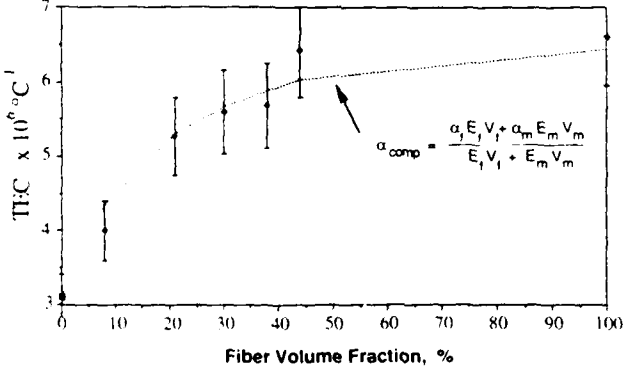

Fig. 5. Effect of fiber volume fraction on the axial thermal expansion coefficients of composites. Dotted line is a plot of Eq. (1) (see text).

(2) *Thermal Expansion of Composites*

The functional dependence of the axial CTE of the composite samples on fiber volume fraction is shown in Fig. 5, where each datum point is the result of at least two or more separate samples at each volume fraction. The dotted line was calculated according to the following:[15]

$$\alpha_{comp} = \frac{\alpha_f E_f V_f + \alpha_m E_m V_m}{E_f V_f + E_m V_m} \qquad (1)$$

where f and m refer to the fiber and matrix, respectively. α_i, E_i, and V_i are the CTE, Young's modulus, and volume fraction, respectively. Figure 5 shows the comparison between the experimental and corresponding predictions using Eq. (1). The agreement between the two is excellent and not only confirms the validity of Eq. (1) in predicting the thermal expansion coefficients of these composites, but also indirectly confirms the value of 6.5×10^{-6} °C^{-1} measured for the fibers.

IV. Summary and Conclusions

(1) The thermal expansion coefficients of SiC monofilaments were measured to be $6.5 \pm 0.5 \times 10^{-6}$ °C^{-1} in the temperature range 200°–900°C.

(2) The linear theory predicting the CTE for unidirectional fiber-reinforced ceramic matrix composites was shown to be satisfactory and indirectly confirms the value of the CTE measured for the fibers.

(3) Heat treatment of the fibers (1400°C, 90 min) resulted in a noticeable increase in the intensity and a sharpening of the β-SiC peak, indicating some grain growth.

(4) The reason for the anomalously high CTE measured for the fibers is not entirely clear, but the XRD results seem to indicate that, possibly, the presence of an amorphous grain-boundary phase in the fibers with a higher CTE than bulk SiC could be responsible.

References

[1] H. E. DeBolt, H. E. Krukonis, and F. E. Wawner, "High Strength, High Modulus SiC Filament via CVD"; p. 168 in *SiC Carbide*. Edited by R. C. Marshall, J. W. Faust, and C. E. Ryan. University of South Carolina Press, Columbia, SC, 1973.

[2] G. Morscher, P. Pirouz, and A. H. Heuer, "Temperature Dependence of Interfacial Shear Strength in SiC-Fiber-Reinforced Reaction-Bonded Silicon Nitride," *J. Am. Ceram. Soc.*, **73** [3] 712–20 (1990).

[3] M. Brun and M. Borom, "Thermomechanical Properties of Chemically Vapor Deposited Silicon Carbide Filaments," *J. Am. Ceram. Soc.*, **72** [10] 1993–96 (1989).

[4] J. DiCarlo, "Creep of Chemically Vapor Deposited SiC Fibers," *J. Mater. Sci.*, **21**, 217–24 (1991).

[5] P. Jero, R. Kerans, and T. Parthasarathy, "Effect of Interfacial Roughness on the Frictional Stress Measured Using Pushout Tests," *J. Am. Ceram. Soc.*, **74** [11] 2793–801 (1991).

[6] R. W. Goettler and K. T. Faber, "Interfacial Shear Stresses in Fiber-Reinforced Glasses," *Compos. Sci. Technol.*, **37**, 129–47 (1989).

[7] J. Bright, S. Danchaivijit, and D. Shetty, "Interfacial Sliding Friction in Silicon Carbide–Borosilicate Glass Composites: A Comparison of Pullout and Pushout Tests," *J. Am. Ceram. Soc.*, **74** [1] 114–22 (1991).

[8] E. P. Butler, E. Fuller, and H. Chan, "Interface Properties For Ceramic Composites from a Single-Fiber Pull-out Test", in *Tailored Interfaces in Composite Materials*, Material Research Society Symposium Proceedings, Vol. 170, Material Research Society, Pittsburgh, PA, 1990.

[9] J. Chou, M. Barsoum, and M. J. Koczak, "Effect of Temperature on Interface Bonding of SiC-Glass Single-Fiber Specimens," *J. Mater. Sci.*, **26**, 1216–22 (1991).

[10] M. Barsoum, P. Kangutkar, and A. S. D. Wang, "Matrix Crack Initiation in Ceramic Matrix Composites: Part I, Experimental and Test Results," *Compos. Sci. Technol.*, **44**, 257–70 (1992).

[11] K. D. McHenery and R. E. Tressler, "Elevated Temperature Strength of Silicon Carbide-on-Carbon Filaments," *J. Compos. Mater.*, **9**, 73–76 (1975).

[12] Z. Li and R. C. Bradt, "Thermal Expansion and Thermal Expansion Anisotropy of SiC Polytypes," *J. Am. Ceram. Soc.*, **70** [7] 445–48 (1987).

[13] F. E. Wawner, A. Y. Teng, and S. R. Nutt, "Microstructural Characterization of SiC (SCS-6) Filaments," *SAMPE Q.*, **14** [3] 39–45 (1983).

[14] S. R. Nutt and F. E. Wawner, "Silicon Carbide Filaments Microstructure," *J. Mater. Sci.*, **20**, 1953–60 (1985).

[15] R. A. Schapery, "Thermal Expansion Coefficients of Composite Materials Based on Energy Principles," *J. Compos. Mater.*, **2** [3] 380–404 (1968).